Absorption Measurements of the Metastable Atom Density in an Atmospheric Pressure Plasma

Master Thesis

in the
Degree Program
"Master of Science"
in Physics

at the Faculty of Physics and Astronomy
of the Ruhr-Universität Bochum

by
Alexander Schicke

from
Kreuztal

Bochum 2024

Abstract

The densities of the He $^3S_1$ and Ar $^3P_2$ metastable states were simultaneously and with high spatial resolution measured using tunable diode laser absorption spectroscopy (TDLAS) in the COST Reference Microplasma Jet, a radio frequency atmospheric pressure plasma jet. The proportion of argon in a helium discharge was varied, as was the power dissipated in the plasma. A particular focus was placed on the development of the spatial distribution of the metastable atoms within the plasma jet, which was made possible by the use of stepper motors to facilitate movement. The data obtained should be used as a reference point for future studies involving the addition of reactive species such as CO_2 to the discharge. The measurements with CO_2 should ultimately provide insights into the dissociation of CO_2 and answer the question of what role metastable atoms play in this process.

The variation in the admixture of argon is accompanied by a rapid decrease in the density of metastable helium and an increase in the density of metastable argon. From an admixture of 0.05%, the density of metastable argon is higher than that of helium. This is due to the lower excitation energy of metastable argon. Further insights are provided by the vertical profiles of the power variations, which demonstrate dynamics at an admixture of 0.1%, in a manner analogous to that observed in pure argon discharges.

Kurzfassung

Es werden die Dichten der He $^3S_1$ und Ar $^3P_2$ metastabilen Zustände mit Absorptionsspektroskopie mittels durchstimmbarer Laserdioden (TDLAS) simultan und höher räumlicher Aufläsung im COST Reference Microplasma Jet, einem radiofrequenz Atmosphärendruckplasma, gemessen. Dabei wurde der Anteil von Argon in einer Heliumentladung variiert, sowie die im Plasma dissipierte Leistung. Ein Augenmerkt wurde dabei auf die entwicklung der räumlichen Verteilung der metastabilen Atome im Plasmajet gelegt, was durch eine Verschiebung dieses durch Schrittmotoren ermöglicht wurde. Die Messung sollen als Vergleich zu Messungen dienen, bei denen zusätzlich reaktive Spezies, wie CO_2, zu der Entladung zugefügt werden. Die Messungen mit CO_2 sollen letztendlich Einblicke in die Dissoziation von CO_2 geben und die Frage beantworten, welche Rolle metastabile Atome in dieser spielen.

Die Variation der Beimischung von Argon zeigt eine rapide Abnahme der Dichte von metastabilem Helium und eine Zunahme der Dichte von metastabilem Argon. Ab einer Beimischung von 0.05% ist die Dichte von metastabilem Argon höher als die von Helium, was an der niedrigeren Anregungsenergie von metastabilem Argon liegt. Weitere Einblicke liefern die vertikalen Profile der Leistungsvariationen, die bei einer Beimischung von 0.1% dynamiken zeigen, wie sie bei reinen Argonentladungen der Fall sind.

Contents

1. Introduction

In the plasma community, the dissociation of CO_2 has become a growing topic over the last years. There are many applications, including decarbonising the atmosphere and producing hydrocarbons for chemicals and fuels [1, 2].

Stewig et al [3] investigated the conversion of CO_2 in a helium atmospheric pressure rf plasma [4] for different argon admixtures in the feed gas. In figure 1.1a one can see that adding only CO_2 into the feed gas results in dissociation degrees of about 45%. This is increased with argon in the feed gas up to 85% in a pure argon plasma.

The power dissipated in the plasma has also a big influence on the CO_2 conversion as visible in figure 1.1b. At low powers (up to 1 W), the conversion of CO_2 is approximately the same for all argon admixtures. This changes at higher powers. For example, at about 4.5 W the conversion rises by 40% for a pure helium plasma. For an argon admixture of 10%, the conversion rises by 60%. Both, the argon admixture and the plasma power play a big role in the conversion of CO_2.

It was assumed, that two of the main reaction pathways responsible for the dissociation of CO_2 are electron impact dissociation and dissociation via Penning collisions with metastable atoms.

To quantify how big of a role the metastable atoms play in the dissociation of CO_2 one needs to measure the dynamics of the helium and argon in a discharge without CO_2 as a benchmark for further measurements. This is done in this thesis. A controlled admixture of argon to a helium discharge is applied while simultaneously observing both metastable atom densities spatially resolved.

The applied plasma source is the COST Reference Microplasma Jet [5]. This atmospheric pressure plasma was developed to be able to compare results between many research

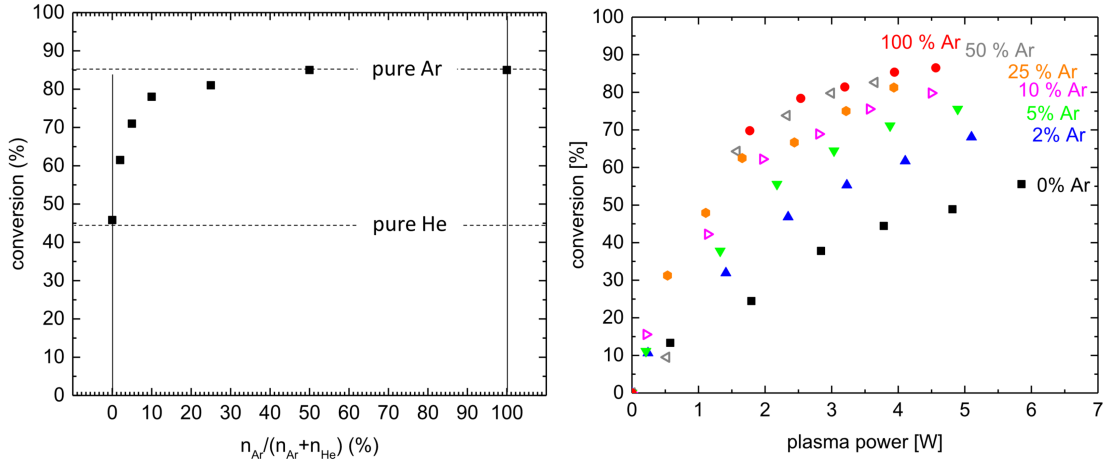

Figure 1.1: CO_2 conversion in a helium atmospheric pressure rf plasma for different (a) argon admixtures and (b) plasma powers with an admixture of 0.125% CO_2 from [3].

groups with standardised conditions of the discharge. Atmospheric pressure plasmas have the advantage that no vacuum chamber is needed and therefore materials which are not compatible with vacuum can be treated. Additionally, the low gas temperature of rf plasmas enables the treatment of temperature-sensible materials like human skin [6].

With the small dimensions of the plasma jet invasive diagnostics to measure the metastable atom densities are impracticable. The fact, that metastable atoms are neither charged nor distinguishable by mass from their ground-state atoms makes the measurements even harder. Emission spectroscopy is also not practicable due to the long lifetimes of these species.

The diagnostics used in this thesis is tunable diode laser absorption spectroscopy. In this diagnostics, the metastable atoms are excited with the radiation of a tunable laser diode. These tunable laser diodes can tune the laser frequency in the range of GHz enabling the scanning of single transition lines. From the proportion of the absorbed light, the density of the species can be calculated. Because only relative intensities are needed, a calibration is not necessary. An additional advantage is that low concentrations can be measured because of the usage of a high-power coherent light source.

The measurements of two-dimensional helium and argon metastable atoms maps are nothing new, even in the own research group [7, 8]. What distinguishes this work from previous research is the plasma source, in which metastable atom densities have not been measured and the simultaneous measurement of helium and argon metastable atom profiles, which requires the excitation of both metastable states by different lasers, subsequently needs a significant change of the typical setup and facilitates detailed insights in the dynamics of these metastable atoms.

2. Fundamentals

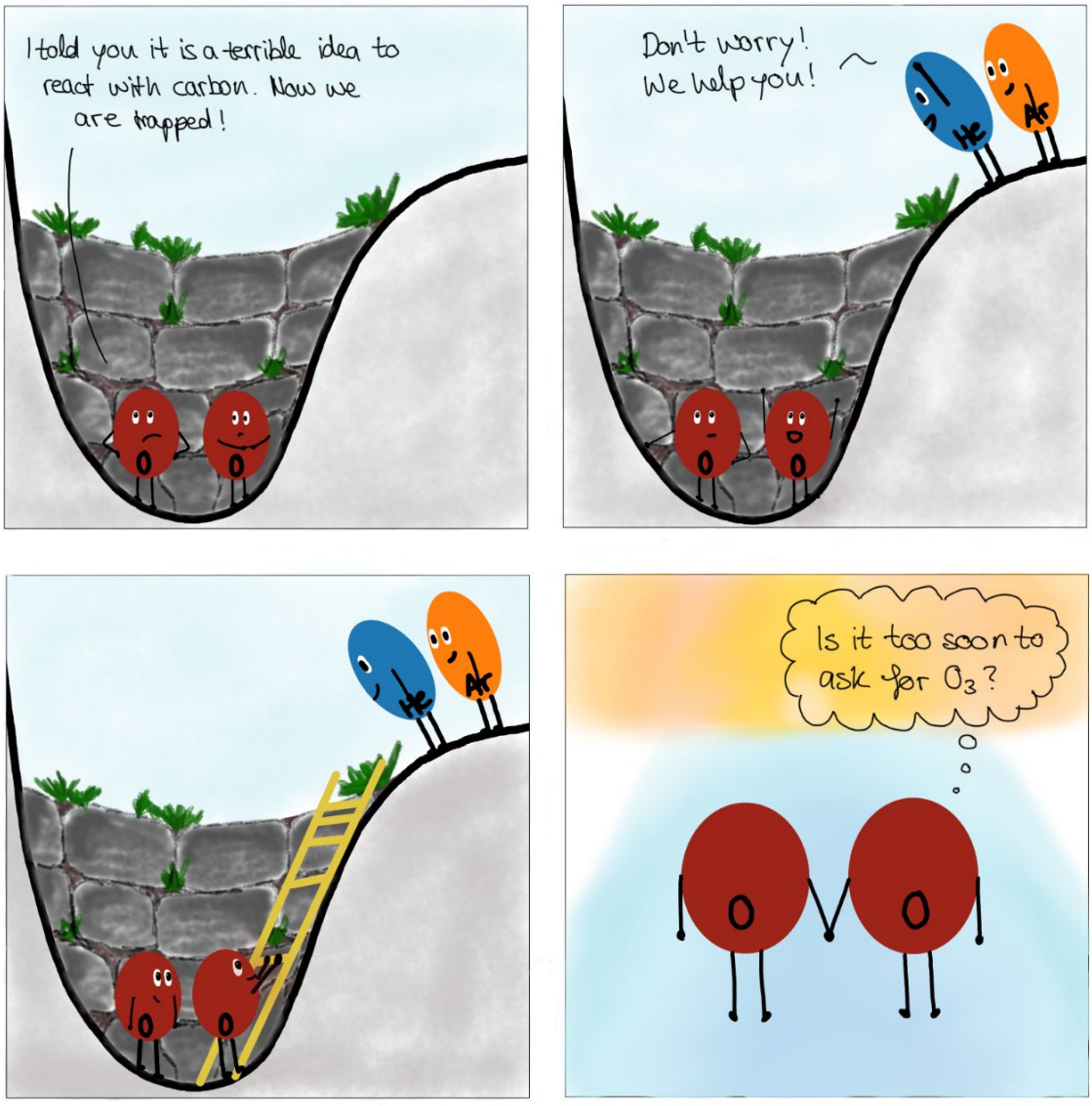

2.1 Atmospheric Pressure Plasmas

A plasma is an ionised gas that shows collective behaviour. The principle of operation is relatively simple. The ignition of a direct current discharge (DC) is described in the following section. An RF discharge operates in a slightly different manner and is described in the subsequent section (2.1.1).

Two electrodes are placed in a gas, and a direct current voltage is applied to the electrodes. This voltage accelerates free electrons in the gas, which ionises particles from the gas via collisions, creating more and more electrons and ultimately an avalanche of electrons. This phenomenon is described by the current that arrives at the anode

$$I = I_0 \cdot \exp(\alpha d) \tag{2.1}$$

with the initial current at the cathode, I_0, and the distance between the electrodes, d. The first Townsend coefficient α describes the number of electrons produced per unit length due to ionisation.

However, for a self-sustaining plasma to operate, new electrons must constantly be generated at the cathode. This is the case because the ions created by the ionisation process are accelerated towards the cathode, where they hit the cathode and produce secondary electrons. The second Townsend coefficient γ describes the number of secondary electrons released per ion that hits the cathode. For the plasma to maintain its operation, each electron must now produce at least one electron. This is described by the ignition criterion

$$\gamma[\exp(\alpha d) - 1] = 1. \tag{2.2}$$

This condition can also be employed to establish an ignition criterion for the requisite voltage applied to the electrodes

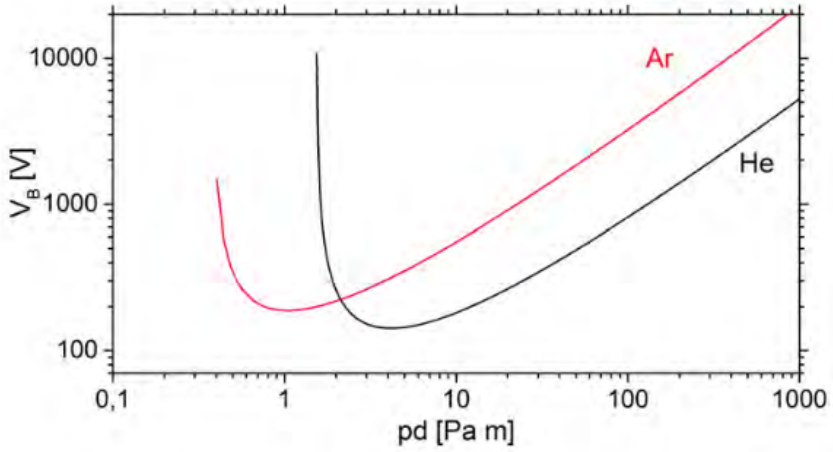

Figure 2.1: Paschen curves of argon (red) and helium (black) from [10].

$$V = \frac{Bpd}{\ln(Apd) - \ln[\ln(1+\gamma^{-1})]}. \tag{2.3}$$

The equation results in the Paschen curve, as illustrated in figure 2.1 [9]. For large values of the product of the electrode gap d and pressure p, the required ignition voltage increases. This is because a higher voltage is needed to maintain the electric field strength, and the time between impacts becomes shorter at high pressure. Consequently, the electrons still have to absorb the ionisation energy in a shorter time. The ionisation energy is contained in the factor B, which also influences the ignition voltage. If the value of pd is too small, ignition is difficult because the electrons cannot absorb enough energy over a too short distance and cannot find enough impact partners. However, some effects nevertheless enable ignition, for example, field ionisation [9]. The lower limit is determined by the second Townsend coefficient γ and the factor A, which depends on the electrode material.

However, in plasmas operated at atmospheric pressures, the generation of electrons is so high that they can shield the external electric field and a streamer forms. This occurs when the avalanche's local electric field becomes similar to the external field. This local electric field can now fulfil the ignition condition and thus propagate. A quasi-neutral

channel is left behind, which can generate an arc as soon as the streamer and the ionisation wave it generates hit the electrodes [11].

The release of high temperatures and the flow of high currents during the arc can damage the electrodes and the electrical components. Therefore, it is important to prevent this, unless the generation of a plasma is desired under precisely these conditions. There are several ways to prevent this short circuit. One method is to install a dielectric between the electrodes and the plasma, the dielectric barrier discharges (DBD). Furthermore, the usage of helium prevents these because of its high thermal conductivity.

2.1.1 COST-Jet

To remain in the regime where one needs low voltages for ignition at atmosphere pressures one needs to use microplasmas with small distances between the electrodes. One of these microplasmas is the COST Reference Microplasma Jet (COST-Jet) [5]. This plasma jet is a capacitively coupled, coplanar rf plasma. A gas flows vertically between the electrodes. An alternating voltage with a frequency of 13.56 MHz is applied to the electrodes. This frequency ensures that the inert ions, in contrast to the electrons, cannot follow the changing field and remain at approximately room temperature [12]. As the electrons are not only accelerated by the alternating field but also repeatedly decelerated, ignition and heating in an RF plasma work slightly differently from the DC plasma described above.

Without collisions, electrons would move in phase with the alternating electric field and would not gain any energy on average. However, collisions with neutral gas particles cause electrons to change phase with the electric field, resulting in a gain of energy on average. The loss of electrons occurs here through diffusion to the walls. An electron must generate at least one new electron before it is lost at the wall for ignition. The ignition curve is comparable to that of the DC case but requires lower voltages of several hundred volts, which dissipate up to several watts of power in the plasma. However, the plasma transitions into constricted mode at high voltages [13].

The COST jet design exhibits several advantages over other plasmas. The atmospheric pressure eliminates the need for vacuum chambers. The RF frequencies maintain the gas temperature at room temperature, enabling applications such as direct skin contact for medical and biological research [14, 15, 16]. The coplanar arrangement of the electrodes allows the easy installation of windows, thus facilitating optical diagnostics of the plasma.

2.1.2 Operation Modes

The application of a voltage allows for the differentiation of plasmas into several distinct heating modes, which are also observable in the discharge itself. For the description of an atmosphere pressure rf discharge, these are the Ω and Penning modes.

Ω mode: At low voltages in helium rf discharges at atmospheric pressure ionisation is caused by high electric drift fields in the bulk during the expansion and retreat of the sheath in an rf cycle. These fields are caused by the low conductivity due to high electron-neutral collisions and therefore named Ω mode after the ohmic heating process [17, 18]. In a pure argon plasma, this mode is not observed [19].

Penning mode: At higher voltages, the discharge transitions into a γ-like mode. This is characterised by the creation of secondary electrons by ion impact at the electrodes. However, in atmosphere pressure plasmas the majority of new electrons are created by stepwise ionisation and Penning ionisation at the sheaths [20]. Therefore this mode is also called Penning mode.

2.2 Metastable Atoms

Metastable atoms are created by electron impact excitation. While most states deexcitate to the ground state (directly or indirectly), this is not permitted for metastable states due to the constraints of quantum mechanical selection rules [21]. Consequently, the lifetimes of metastable states at atmosphere pressure are up to microseconds long and longer than those of other states (the lifetimes can get up to hours in low pressures). This is because they can only deexcite through diffusion to the walls of the plasma chamber or collisions [22]. Consequently, they act as an energy store in the plasma, which can be

used for various other reactions [23].

In plasmas with higher pressures, such as atmospheric pressure plasmas, the electrons can absorb less energy through the electric field due to the short time between collisions. Consequently, the energies required for direct impact ionisation are too high. In this work helium with an ionisation energy of 24.6 eV and argon with 15.8 eV are being used [9]. There a different ionisation process is of more importance, the stepwise ionisation. The electrons first excite an atom and another electron subsequently ionises this already excited atom. Therefore the required ionisation energy is split onto two electrons and the overall required energy of a single electron is lower. This process is dependent on the electron density and the lifetime of the state of the excited atom, which is why metastable atoms play an important role in the discharge dynamics for reactive processes.

Analogous processes include Penning ionisation, in which a metastable atom collides with a molecule (such as CO_2) and ionises it,

$$X^m + CO_2 \rightarrow X + CO_2^+ + e^- \tag{2.4}$$

and Penning dissociation, in which the energy of the metastable state leads to dissociation of the molecule [24]

$$X^m + CO_2 \rightarrow X + CO + O. \tag{2.5}$$

The dissociation of carbon dioxide into carbon monoxide and oxygen is one example of the numerous decay channels of CO_2. It is also possible for the molecule to dissociate and ionise simultaneously, in which case one atom of the decomposition is ionised.

The metastable states investigated in this work are those with the lowest potential energy for their respective species, with values of 19.8 eV for helium and 11.5 eV for argon (see term diagrams in figure 2.2). These states are the metastable states with the highest density and exceed the required dissociation energies of about 5.5 eV for CO_2 by a signi-

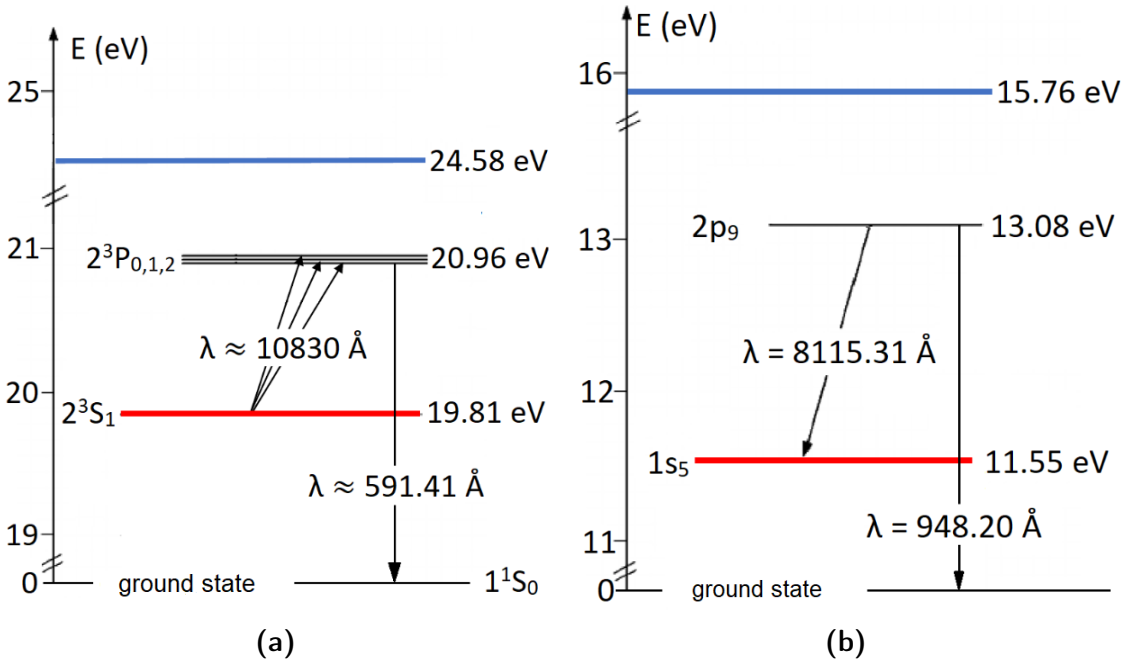

Figure 2.2: Term diagram of the important (a) helium and (b) argon states (the argon transition is in Paschen notation) adapted from [7].

ficant margin [25]. All necessary information for the helium and argon transitions are in Table 2.1.

The quenching rates of nitrogen and oxygen on helium and argon are exceptionally high [27]. Consequently, the atmosphere profoundly influences the discharge, as more ambient air enters the discharge channel at a lower flow rate through back diffusion. This

	Transition	Central Wavelength	Oscillator strength	Lower State Energy	Upper State Energy
He^m	$2^3S_1 \rightarrow 2^3P_1^0$	1083.025 nm	0.18	19.82 eV	20.96 eV
He^m	$2^3S_1 \rightarrow 2^3P_2^0$	1083.034 nm	0.30	19.82 eV	20.96 ev
Ar^m	$1s_5 \rightarrow 2p_9$	811.531 nm	0.46	11.55 eV	13.08 eV

Table 2.1: List of the studied transitions with their wavelength and oscillator strength (the argon transition is in Paschen notation) [26].

effect is particularly pronounced at the walls due to the slower flow rate there [28]. This phenomenon can be observed in the two-dimensional maps (see section 5). To prevent quenching to the greatest extent possible, helium and argon gases with a purity of 99.999% are employed and all pipes were flushed before measurements because water and ambient air deposits there when the gas flow is turned off.

2.3 Absorption Spectroscopy

The diagnostic methodology employed to determine metastable densities in this thesis is tunable diode laser absorption spectroscopy (TDLAS). When a laser beam passes through a plasma, a portion of the initial intensity, designated as I_i, is absorbed by the plasma as a result of excitation. The final intensity, designated as I_f, is lower than the initial intensity. This phenomenon can be expressed by the Beer-Lambert law

$$I_f(\nu) = I_i(\nu)e^{-\alpha(\nu)l} \tag{2.6}$$

where $\alpha(\nu)$ is the absorption coefficient and l is the path length of the laser through the plasma.

The absorption coefficient is defined as

$$\alpha(\nu) = k_0\Phi(\nu)\left(n_l - \frac{g_l}{g_u}n_u\right) \tag{2.7}$$

with n_l and n_u being the densities of the population of the lower and upper states. In this case, the lower state is the metastable state, whose density is much higher than the upper state density ($n_l \gg n_u$). $\Phi(\nu)$ is the normalised line profile resulting from the different broadening (more on this in section 2.3.1). The constant k_0 is defined as follows [29]

$$k_0 = -\frac{1}{4\pi\epsilon_0}\frac{\pi e^2}{m_e c} f_{lu} \tag{2.8}$$

where $f_{lu} = -f_{ul}$ is the oscillator strength of the line, which is the proportion of the transition $l \to u$ in respect to all other energy state transitions to u [30].

With this and eq. 2.7 one can adjust eq. 2.6 into

$$\ln\left(\frac{I_f(\nu)}{I_i(\nu)}\right) = \frac{1}{4\epsilon_0}\frac{e^2}{m_e c} f_{lu}\Phi(\nu) n_l l. \tag{2.9}$$

To get the mean density we integrate both sides and rearrange:

$$\langle n_l \rangle = 4\epsilon_0 \frac{m_e c}{e^2 f_{lu} l} \int \ln\left(\frac{I_f(\nu)}{I_i(\nu)}\right) \mathrm{d}\nu \tag{2.10}$$

The integral over the line shape $\Phi(\nu)$ is equal to one, because it is normalised ($\int \Phi(\nu)\mathrm{d}\nu = 1$).

One has to consider that some of the laser intensity will stray away and one gets background radiation onto the detector. So one has to adjust the formula and do some more measurements

$$\frac{I_i(\nu)}{I_f(\nu)} = \frac{I_L - I_B}{I_{PL} - I_P} \tag{2.11}$$

with

- I_B being the intensity of background radiation, so laser off, plasma off
- I_L being laser on, plasma off
- I_P being laser off, plasma on
- I_{PL} being laser on, plasma on

With this, one can form the final formula for the mean density

$$\boxed{\langle n_l \rangle = 4\epsilon_0 \frac{m_e c}{e^2 f_{lu} l} \int \ln\left(\frac{I_{PL} - I_P}{I_L - I_B}\right) \mathrm{d}\nu.} \tag{2.12}$$

Note that using the Beer-Lambert law assumes a homogeneous plasma, which is only partially true. As explained in section 2.1.2 the plasma is not homogeneous because of the very different densities in the sheath and bulk, but the laser penetrates only a small portion of the plasma, due to the finite beam width. Along the beam, we assume the plasma to be homogeneous as will be seen in chapter 3. This version of the Beer-Lambert law is also just for a single line, which is what is measured here. To measure multiple lines, one must add an exponent with the corresponding absorption coefficients.

For this method to be employed, the laser must be capable of scanning the individual absorption peaks. For this to be achieved, the frequency (or wavelength) of the laser must be smaller than the width of the transition, which means that it must be tunable in the GHz range. Conversely, TDLAS does not require any calibration of the intensities, as only relative intensities are employed, nor does it require an absolute calibration of the wavelength.

2.3.1 Line Broadening

Despite the frequency of a photon emitted from an energy state E_u to a lower state E_l being well defined as $\nu = (E_u - E_l)/h$ (with h being the Planck constant), the spectral absorption line has a certain width as seen in figure 2.3. Depicted are the helium transitions excited by the laser in this work. These transitions are only 2.67 GHz apart and due to broadening effects, these cannot be resolved individually. Nevertheless, their relative intensities are taken into account to determine the densities. This line broadening can be the consequence of a variety of effects, which some fundamental and some important ones for atmospheric pressure plasmas will be discussed below.

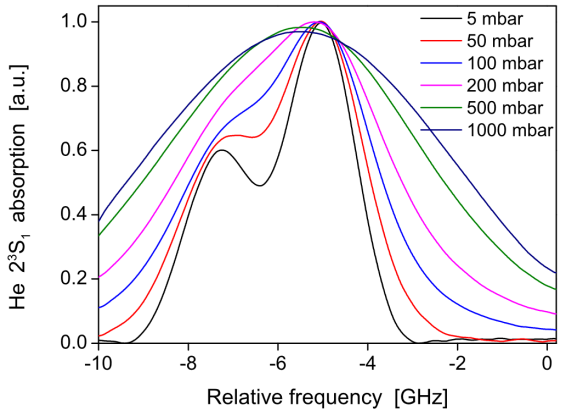

Figure 2.3: Absorption line profile of the He^m transitions under pressure variations from [31].

Natural Linewidth

The most fundamental broadening effect, the natural line width, is due to the natural lifetime τ of an exited state E. This comes from Heisenberg's uncertainty principle. The mean lifetime of τ has an uncertainty of $\tau \Delta E \geq \hbar$ [32]. This translates with $E = h\nu$ to

$$\Delta\nu = \frac{\Delta E}{h} = \frac{\hbar}{h\tau} = \frac{1}{2\pi\tau}. \tag{2.13}$$

Note, that this is only true if the emission is into the ground state, otherwise one has to take both lifetimes of both excited states into account.

The shape of this broadening mechanism is a Lorentz profile

$$\Phi_n(\nu - \nu_0) = \frac{1}{2\pi} \frac{\gamma_n}{(\nu - \nu_0)^2 + \left(\frac{\gamma_n}{2}\right)^2} \qquad \text{with} \quad \int_0^\infty \Phi_n(\nu) \mathrm{d}\nu = 1 \tag{2.14}$$

where $(\nu - \nu_0)$ is the deviation from the line centre and γ_n is the FWHM (full width at half maximum)

$$\gamma_n = 2\pi\Delta\nu = \frac{1}{\tau}. \tag{2.15}$$

From this, one can see that with a higher lifetime, the distribution width gets smaller and since metastable transitions are measured, which have a high lifetime, this effect can be neglected [30].

Collisional Broadening

The presence of other particles changes the wavelength of an emitted photon. This can happen in two limiting cases, depending on whether the collision itself is faster than the emission or not.

Suppose the collision is faster than the emission. In that case, the collision interrupts the emission. It changes the effective lifetime of the state, which, like the natural linewidth, results in a change in frequency due to the uncertainty principle. For this to happen, the gas atoms need high velocity and therefore small densities to have time to accelerate. In an atmospheric pressure plasma like the COST-Jet, neither is the case.

The most significant broadening effect for these measurements is the quasi-static pressure broadening, for a collision time much shorter than the emission. In this case, one can interpret the perturber with a potential of the form

$$\Delta E \sim r^{-n} \tag{2.16}$$

with r being the distance to the perturbed. For different interaction species and forces, n has different values:

n=2 is the case for excited hydrogenic atoms interacting with electrons or ions. It results in a Stark shift in the energy levels.

n=4 is the quadratic Stark broadening between e.g. excited helium with electrons and ions.

n=3 is a resonance dipole-dipole interaction between an excited atom and another atom of the same species (only neutrals)

n=6 is long-range van der Waals dipole-dipole interaction between an excited atom and another atom of any species (this is always the case)

Both Stark broadening effects occur in highly ionised gases and with strong external electric fields. For low ionised gases resonance and van der Waals broadening are most significant [33]. This broadening effect has also the form of a Lorentzian.

Doppler Broadening

All neutral particles in the plasma are moving randomly. Excited particles emit photons, whose frequency is slightly shifted due to the Doppler effect, depending on the direction of the excited particles. The shift depends on the gas temperature T_g, the mass of the observed gas particles m_g and the unshifted wavelength λ_0

$$\Delta\nu_D = \lambda_0^{-1}\sqrt{8\ln(2)\frac{k_b T_g}{m_g}}. \tag{2.17}$$

For the helium line at room temperature, this shift is less than 2 GHz [34]. This broadening effect has the form of a Gaussian.

We are going to neglect this broadening mechanism in the data evaluation because it is one order smaller than the combined Lorentzian effects [8].

3. Setup

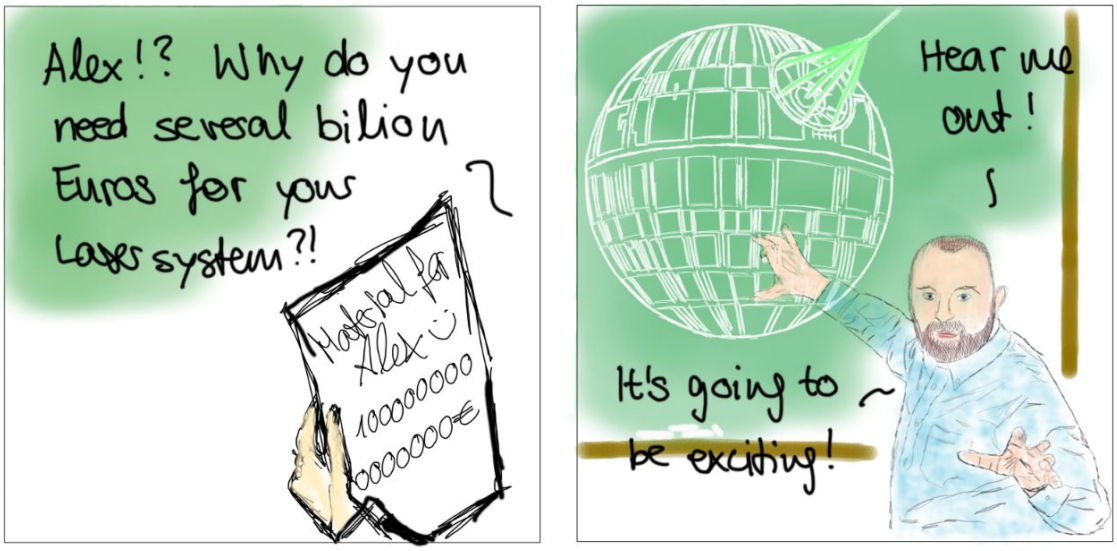

An overview of the experimental setup is provided in figure 3.1. The centre of the diagram depicts the used plasma source, the COST Reference Microplasma Jet (see section 3.1). Two lasers are required to simultaneously measure helium and argon metastable atoms (see section 3.4), which excite the respective metastable atoms. Furthermore, the devices were almost always controlled using a self-made LabView programme. The specific devices and the manner of their control can be found in the respective sections. However, the LabView code is far too large to be reproduced here.

3.1 The COST Reference Microplasma Jet

As previously stated in the fundamentals section, the COST Reference Microplasma Jet (COST-Jet or just plasma jet) is a capacitively coupled low-temperature plasma. Figure 3.2a depicts the plasma jet with ignited plasma. The housing contains the current and

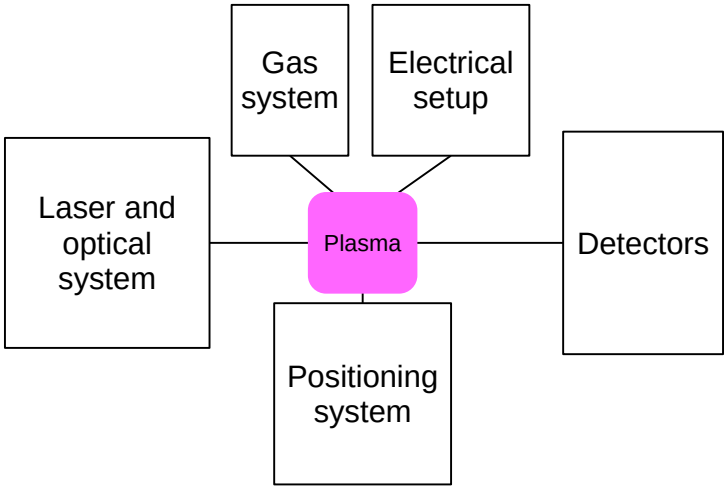

Figure 3.1: Block diagram of the setup.

voltage probe, while the external connection to the power supply is located at the rear end. The head (see figure 3.2b) comprises two electrodes, one driven with an AC voltage of 13.56 MHz and the other grounded. The voltage is regulated by an LC resonant circuit, which serves as a matching box. The 1 mm x 1 mm x 30 mm discharge channel in which the rf plasma is ignited is located between the electrodes. The head is equipped with quartz windows affixed to both sides to facilitate optical diagnostics.

Figure 3.3a illustrates the connections between the power supply via a matching network and the probes to the oscilloscope. The power supply is connected to a laptop via a National Instruments I/O device of type USB-6008, and its operation is controlled via the LabView program previously mentioned. This configuration does not permit the user to set different power levels; rather, these must be set manually between measurements. However, it does permit the user to switch the power on and off as required on multiple occasions during a measurement.

To ascertain the power dissipated in the plasma, an oscilloscope (Teledyne LeCroy HDO6104a) is connected to the current and voltage probes of the plasma jet. The voltage U corresponds to the drop across the electrodes, and the current is calculated from this with an internal resistance of $R_m = 4.7\ \Omega$. It is necessary to take the internal

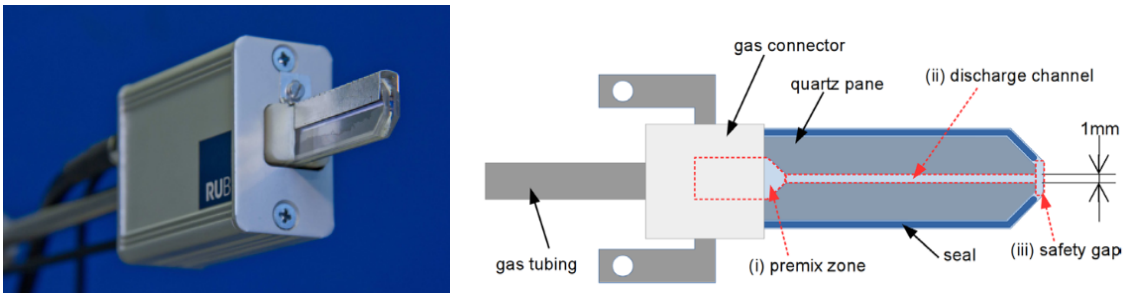

(a) (b)

Figure 3.2: (a) Photograph of the ignited COST-Jet and (b) a sketch of the head including the discharge channel adapted from [5].

resistance of the cable, $R_t = 50\ \Omega$, into account here, to calculate the current [5]

$$I = U\frac{R_m + R_t}{R_m R_t}. \tag{3.1}$$

The power P was calculated using the phase shift method, as outlined in [35], in conjunction with the COST Power Monitor [36]

$$P = U \cdot I \cdot \cos\varphi. \tag{3.2}$$

The COST Power Monitor is a Python-based programme and, as such, represents the sole interface that is not formed by the aforementioned LabView program. Attempts were made to determine the power via the LabView programme, but LabView is too slow to determine the phases correctly.

3.2 The Gas System

The metastable density is dependent upon both the flow velocity of the gas and the presence of impurities within the gas. Concerning the latter, the working gases employed are helium and argon, both of which are of a purity of 99.999%. In particular, at the tip

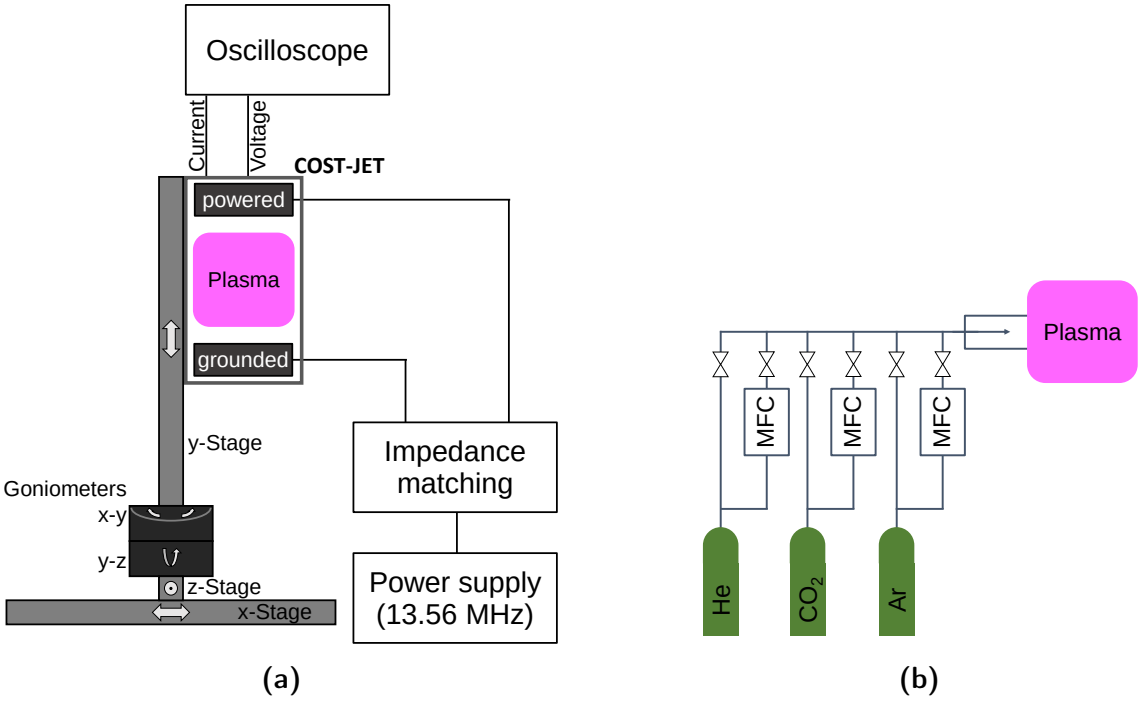

Figure 3.3: Schematic representation of the (a) plasma source including the positioning system and the electronic setup and (b) gas system.

of the plasma jet, the atmosphere penetrates the plasma jet and distorts the densities of the metastable atoms, as will be demonstrated later [28].

The total flow is maintained at 1000 standard cubic centimetres per minute (sccm) for all measurement series. Mass flow controllers (MFC) of the 358 series from Analyt-MTC are installed downstream of the gas line to ensure a constant flow rate and are depicted in figure 3.3b. In the downstream direction, they have a maximum flow rate of 2000, 500 and 20 sccm. The flows can be regulated with a precision of 1%. Bypasses are fitted around each mass flow controller to flush the stainless steel lines. The mass flow controllers are connected to a stainless steel line that is routed to the plasma jet via a flexible stainless steel hose. Valves are installed behind both the mass flow controllers and the bypasses.

The mass flow controllers can be controlled via the LabView programme.

3.3 The Positioning System

The optical components of the apparatus are fixed in place on an experimental table, while the plasma jet is mounted on a holder with three stepper motor stages of the X-LSM100A type from Zaber. These enable the jet to move in all three spatial directions within a range of 100 mm. The stages are controlled via the Labview programme with a micro-stepping accuracy of less than 0.3 microns, thus enabling the plasma jet to be examined spatially. In addition to the aforementioned three stages, a further stage is situated between the collimator lens and the focusing lens in the optical setup. At this stage a shutter is installed, which can be moved into the laser beam paths as required, controlled via the LabView program.

The coordinate system of the stages is depicted in figure 3.3a. The z-axis facilitates the movement of the jet in a parallel direction to the lasers, as is required, for instance, for the varying distances to the focusing lens when determining the beam width (see section 4.1). The y-axis represents the vertical movement perpendicular to the lasers, while the x-axis represents the horizontal movement perpendicular to the lasers. The coordinates of the stages are labelled in the respective plots.

Additionally, two goniometers (Thorlabs XRNG 1/2) are situated beneath the plasma jet, enabling the zenith angles in the y-z plane and the x-y plane to be adjusted. These serve to guarantee that the jet is moved precisely horizontally in the x-direction by the stages and that the maximum gap between the electrodes is utilised, thus preventing the light from being cut off by the electrodes of the plasma jet.

3.4 The Laser and Optical System with the Detectors

To study metastable atoms via TDLAS, an optical setup has been constructed under the specifications outlined in figure 3.4. This apparatus comprises two laser diodes (Toptica Photonics DFB pro L) acting as radiation sources, which are connected to a laser control-

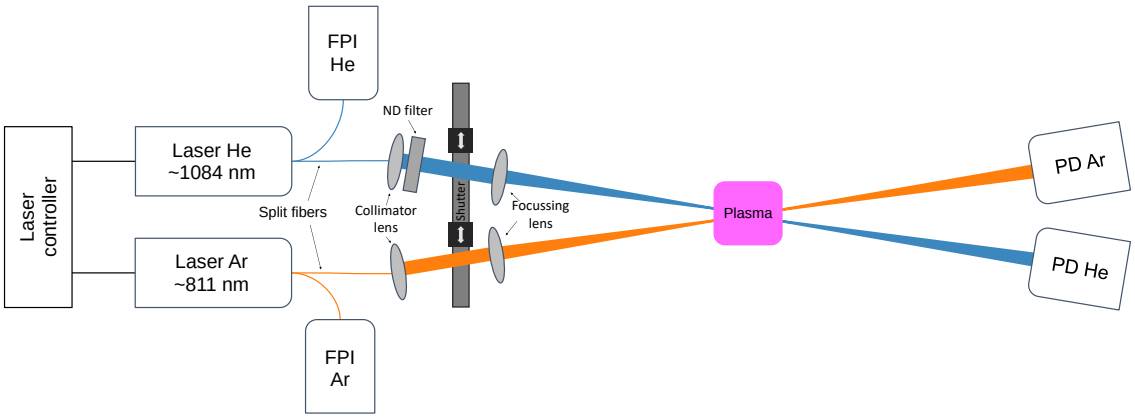

Figure 3.4: Schematic representation of the optical system.

ler (Toptica Photonics DLC pro) capable of regulating the laser diodes. In the following, the laser diodes that excite the respective metastable atomic species are labelled with the respective species (helium and argon laser). The laser controller can also be used as an oscilloscope and thus is connected to the two photodiodes (PD) by Thorlabs of type DET 10C/M (700-1800 nm) in the helium case and DET A/M (200-1100 nm) in the argon case, which measures the attenuated intensities of the laser signals. The controlling of the laser diodes via the laser controller was done with the LabView program, which also received the photodiode signals for further processing.

Each laser diode is connected to collimator lenses with a Thorlabs TW1064R2A1A wide-band coupler fiber (centre wavelength = 1064 nm; bandwidth = $\pm$ 100 nm) in the helium case and a Thorlabs TN808R2A1 narrowband coupler fiber (centre wavelength = 808 nm; bandwidth = $\pm$ 15 nm) in the argon case. Additionally, two Fabry-Perot interferometers (FPI) are installed for relative wavelength determination, which intercepts part of the laser signal. A focusing lens is mounted behind each of the collimator lenses so that the focal points lie in the discharge channel of the jet, which is located behind the focusing lenses. The photodiodes previously mentioned are situated behind the jet. It is important to note that a grey filter (ND=3) is positioned directly behind the collimator lens of the helium laser, as the intensity of the laser is too high and the photodiode would otherwise become saturated.

In previous studies, a portion of the laser beam was directed through a hollow cathode lamp to ascertain the absolute wavelength. This procedure was conducted initially for each laser, serving to determine the optimal settings for the laser. However, continuous monitoring of the wavelength was not necessary, because the absorption peaks were observed during the measurements and the absolute wavelength plays no role in those measurements.

3.4.1 Semiconductor-Diode Lasers

The following is a brief introduction to semiconductor laser diodes. Since this topic is voluminous and complex, only the information necessary for this work is described here. A more detailed description can be found in [37, 38], which has also been used as a source for this section.

A laser diode is a p-n semiconductor. It is composed of a positively charged region (p) with a deficiency of electrons (holes) and a negatively charged region (n) with an excess of electrons. An electron can recombine from the n region to the p region by emitting a photon, whose wavelength depends on the energy gap between the n and p regions and therefore on the semiconductor material. Pumping is achieved through an electrical current. A high electron density allows for the construction of smaller laser diodes, as the photon intensity amplification is significantly higher than that of other lasers. Additionally, the use of resonate mirrors with a lower reflection index enables a greater number of photons to leave the resonator, thereby increasing the intensity of the light through stimulated emission.

Tunability of a Laser Diode

A diffraction grating, which serves to determine the laser wavelength by selecting a single longitudinal mode, is incorporated into the semiconductor chip of a distributed feedback (DFB) laser diode. The wavelength is altered by varying the pitch of the Bragg grating. This can be achieved by changing the temperature or the current, which also causes a temperature change by ohmic heating. Both parameters also transform the refractive in-

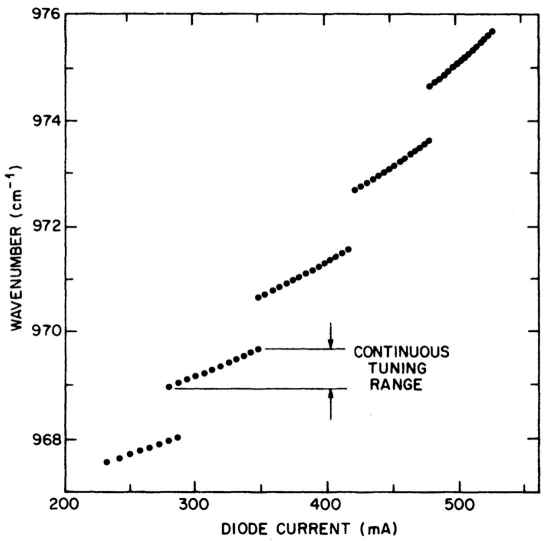

Figure 3.5: Mode hopping when tuning a diode laser via diode current [39].

dex of the semiconductor material, exerting an influence on the wavelength. Furthermore, an increase in current results in a proportional increase in output power and therefore laser intensity, as illustrated in figure 5.1a.

The temperature exerts a greater influence on the wavelength, and in our case, is employed solely for a preliminary adjustment, which is then maintained at a constant level. The current is employed for tuning. The parameters utilized can be observed in Table 3.1, which can be found in the subsequent section.

A change in temperature and a change in current typically result in mode hopping, which is why the frequency can only be tuned linearly in intervals (see figure 3.5). However, the laser system used here is sufficiently advanced to prevent these effects in our frequency ranges (for both lasers), thus eliminating the possibility of mode hopping.

The Used Laser System

The operating parameters of the Toptica Photonics DFB pro L laser heads utilised in this study are presented in Table 3.1. These were controlled by the DLC Pro laser control unit, also manufactured by Toptica Photonics. The scan offset corresponds to the mean

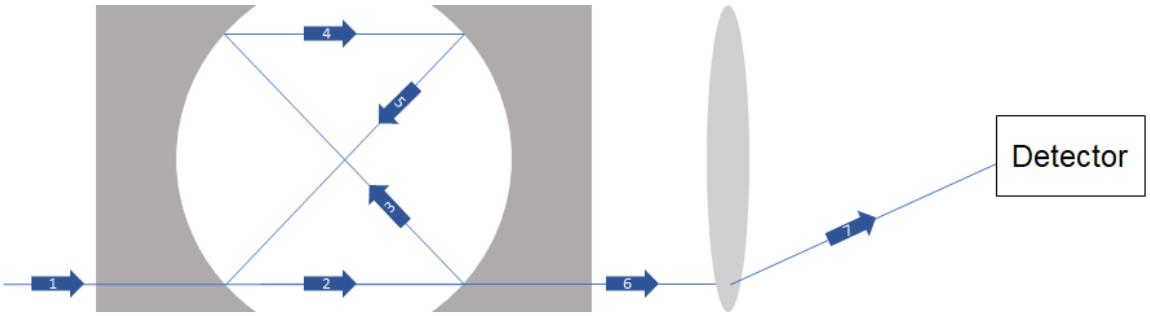

Figure 3.6: The principle of a Fabry-Pérot interferometer.

current with which the laser heads are operated, while the scan amplitude corresponds to the drive ramp. Both ramps were repeated in synchrony at a frequency of 10 Hz. According to the manufacturer, the mode hopping-free range corresponds to up to 1200 GHz.

3.4.2 Fabry-Pérot Interferometer

The intensity of the laser is dependent on the driving current (see figure 5.1a). To calculate the area under the absorption curve (see figure 5.1b) and thus the density, it is necessary to have a frequency-dependent intensity (see equation 2.10). To translate the current change into a frequency change, a confocal FPI with a free spectral range of 1 GHz is employed for each laser. The helium FPI (Toptica FPI 100-0980-3V0) has a

Operating Parameter	Helium Laser	Argon Laser
Temperature	35.7 °C	49.42 °C
Scan Offset	120 mA	36 mA
Scan Amplitude	60 mA	8 mA
Wavelength	1083 nm	811.75 nm
Wavelength Tuning	0.7 GHz/mA 3 pm/mA	8.8 GHz/mA 19pm/mA
Output Power	70 mW	10 mW

Table 3.1: Operating parameters (first three lines) and other manufacturer specifications of the helium and argon laser heads.

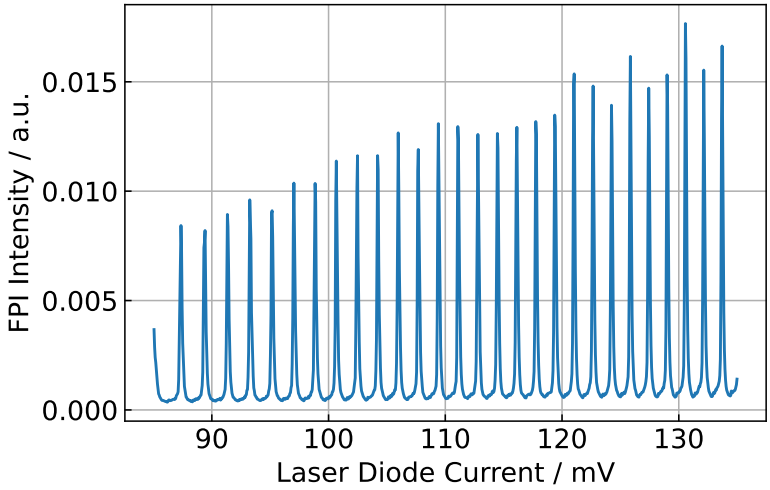

Figure 3.7: Example of the helium Fabry-Pérot interferometer signal.

wavelength range of 825-1200 nm, while the argon FPI (Toptica FPI 100-0750-3V0) has a wavelength range of 615-885 nm.

Figure 3.6 illustrates the principle of a confocal FPI. A laser beam is guided into the device where it is reflected four times by two partially transparent, spherical mirrors until it is again parallel to the input beam. There, the beam interferes either destructively or constructively with the reflected beam, and the resulting intensity is measured by a photodiode. When the frequency of the beam is tuned, a maximum always appears when the frequency meets the resonance condition of the FPI (here 1 GHz) [40, 41]. Figure 3.7 shows an example of an FPI signal as a function of the frequency, in this case, the laser diode current. All of the peaks are 1 GHz apart from each other. With this one can calculate the mean distance between the peaks in mV and then translate the laser diode current-dependent absorption into a frequency-dependent absorption, which then enables the calculation of the area of the absorption peak.

4. Calibration Measurements

The most challenging aspect of the spatially and temporally simultaneous measurement of He and Ar metastable atoms is the adjustment and verification of the optical setup. This involves determining the beam width of the two lasers, which has revealed that the laser beams do not emerge vertically from the collimator lenses. Additionally, the divergence of the focal lenses must be determined, and finally, the alignment must be achieved, whereby the focal points of the lasers pass through the same point in the plasma jet's discharge channel.

4.1 Beam Width and Divergence

To be able to estimate the measured volume and to know how large the overlap of the two lasers is (under optimum conditions), it is important to determine the beam width of the lasers at the focal point of the lenses and their divergence. These were determined using the knife-edge method, as described in [42]. In this method, a knife edge is guided into the laser beam between the focusing lens and the photodiode (see Figure 4.1). As the blade is guided further into the beam, the intensity of light reaching the photodiode decreases until the laser is completely blocked. The intensity measured in the photodiode as a function of the position of the knife edge is shown as an example in Figure 4.2 and follows the following function:

$$I = I_0 + \frac{I_{max}}{2}(1 - \mathrm{erf}\left(\frac{\sqrt{2}(y - y_0)}{w}\right)) \tag{4.1}$$

I_0 represents the intensity of the background, I_{max} the maximum intensity observed. The position of the shift, y_0, is the point at which the intensity has fallen to half of the intensity. The beam's width, w, can be determined by fitting the function. This corresponds to the distance between the maximum and the point at which the intensity

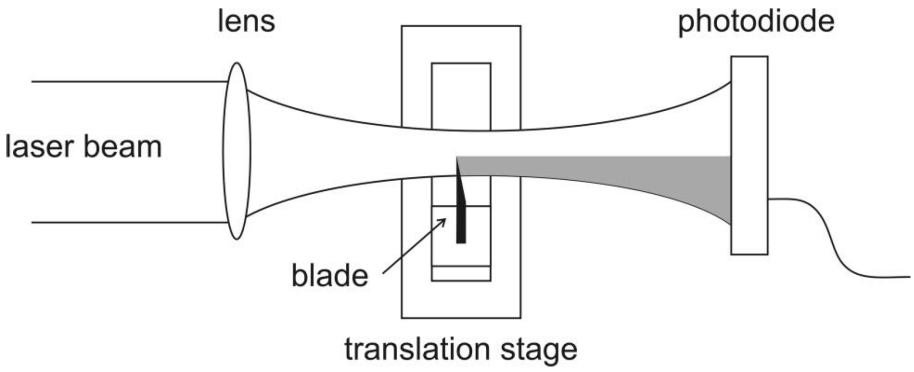

Figure 4.1: The principle of Knife Edge method[42].

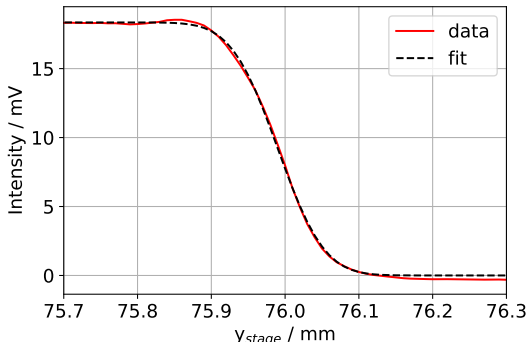

Figure 4.2: Example of a beam width measurement (red) with the fitted function 4.1 (black).

has fallen to $1/e^2$, assuming a Gaussian as the beam profile [43]. We define the point y_0 as the position of the laser for future adjustment.

By varying the distance between the focusing lens and the knife, d, one determines the divergence and the minimum beam width at the focal point. Figure 4.3 shows the beam widths of the lasers for a 40 mm lens in the case of the He laser and a 90 mm lens in the case of the Ar laser for different distances d. At a minimum of approximately 38 microns, the argon laser exhibits a slightly narrower beam width than the helium laser at approximately 65 microns. The lenses were selected to permit offset alignment and to minimise the beam width. The helium laser requires a smaller focal length, as otherwise, the beam width exceeds 120 microns with e.g. an 80 mm lens. It can be observed that

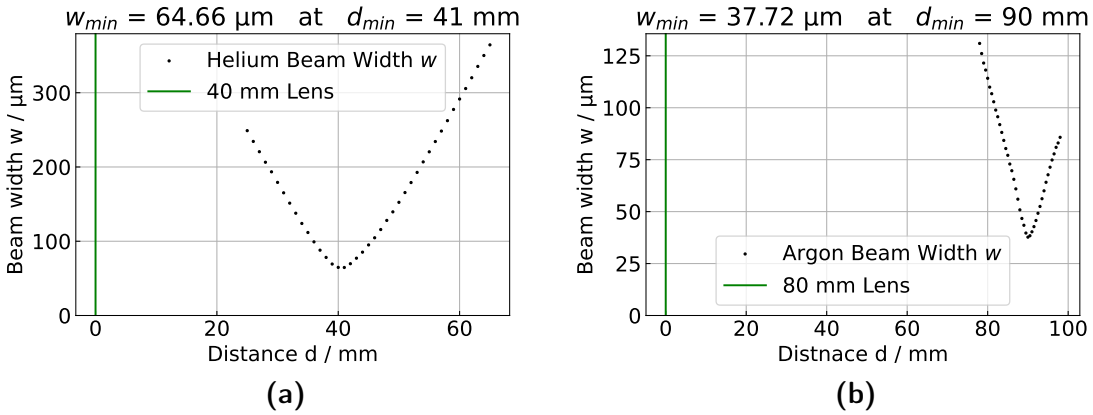

Figure 4.3: Beam width of the (a) helium laser with a 40 mm lens and (b) argon laser with an 80 mm lens depending on the distance to the respective lens d.

the minimum beam width of the argon laser is at a 90 mm distance with an 80 mm lens. However, the reason for this discrepancy is unclear, as the minimum beam width of this lens with the helium laser is observed at an 80 mm distance.

An initial attempt was also made to realise the setup with pinholes, as these simplify adjustment considerably. In this instance, however, the apertures cannot be installed directly in front of the plasma, as the components are too large to allow both laser beams to meet in the plasma at a small enough angle to each other. Consequently, they would have to be installed a few centimetres away from the plasma, which leads to beam widths in the order of 100 microns due to the high divergence. Therefore, the decision was taken in favour of lenses that present a greater challenge in terms of adjustment, but which permit the generation of smaller beam widths at a greater distance from the plasma.

4.2 Fiber and Collimator Lenses

Upon measuring the beam widths, it was observed that the position of the laser varies in height with the distance to the focusing lens, depicted with the stepper stage position z in figure 4.4a. The position of the laser is defined as the point at which the intensity has fallen to 50% of the maximum. The reason for the height variation is that the

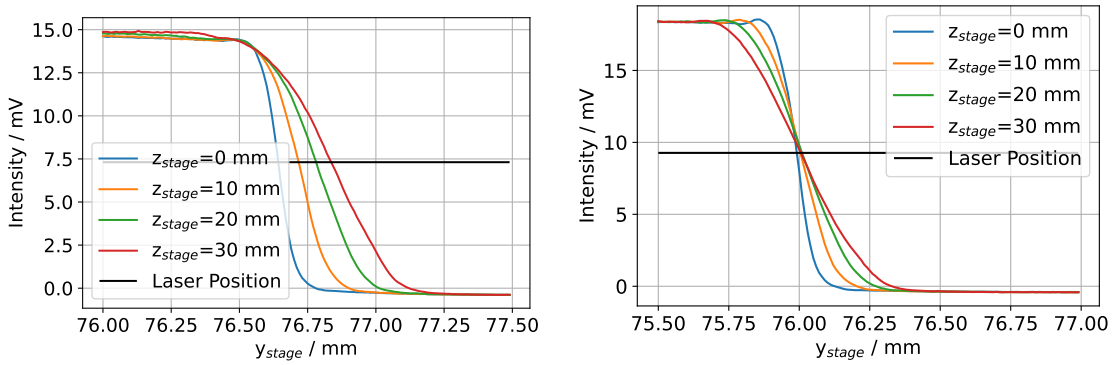

Figure 4.4: Examples of the laser position depending on the distance to the focussing lens at a rotary stage angle of (a) 0° and (b) 120°. The vertical position is indicated in black.

coupling of the optical fibre to the collimator lens is not perfect. As the electrodes of the plasma jet would cut off parts of the light, thereby introducing an additional error into the measurement, this problem was circumvented by inserting the collimator lens into a rotary stage (Thorlabs CRM1T/M). The rotary stage was then adjusted so that the position no longer varied vertically, but only horizontally. However, as the beam is guided into the plasma at a horizontal angle anyway, the system is not disturbed by this. Figure 4.4b illustrates the position of the beam in the vertical plane after correction. It can be observed that the position of the laser is now approximately constant. This was achieved for both collimator lenses, which are ultimately guided through the plasma, as well as for the collimator lenses that guide the lasers into the Fabry-Pérot interferometers.

4.3 Aligning the Lasers

To facilitate a meaningful comparison of the densities of the helium and argon metastable atoms, they must be measured in the same plasma volume. To achieve this, it is necessary to ensure that the beams of the lasers lie as closely together as possible. While this is not entirely feasible, given that the helium laser is wider than the argon laser (see section 4.1), and the beams are not parallel but are at an angle to each other

due to the structure, it is possible to make a meaningful comparison. An alternative approach would have been to completely parallelise the beams using mirrors. However, this was not pursued in this work to avoid further complicating the alignment process. Furthermore, due to the symmetry of the plasma jet, the angle should not influence the density measurements. Nevertheless, as the jet does not have to be perfectly assembled, an attempt was made to minimise the angle between the beams.

The process of aligning the lasers proved to be particularly time-consuming. The collimator lenses, focusing lenses and photodiodes had to be aligned manually. The respective signals of the helium and argon lasers had to be maximised and the beams had to intersect at the focal point of the focusing lenses. The deviation of the position in the focus must be smaller in both the x and y directions than the beam width of the smaller beam (i.e. the argon beam). This is particularly crucial in the x-direction, as opposed to the y-direction. For the majority of the measurement, only vertical slices of the discharge channel were made. This implies that if the alignment in the x-direction is too large, in the most extreme case, entirely disparate volumes may be measured, which could have a significant impact on the density depending on the position inside the discharge channel (see section 2.2). This is also the case in the y-direction, but as the entire plasma is scanned in this direction, the same volume is measured at a subsequent measuring point, which can be rectified during the analysis process. This is also suboptimal, as the plasma can change between the measurement points. However, this is less problematic than in the horizontal case.

Figure 4.5a illustrates the vertical alignment. The knife edge was no longer employed in this instance; instead, the plasma jet was utilised. The electrodes are positioned at the points where the laser intensity is zero, and the discharge channel through the quartz windows can be observed in the centre. At the lower stage coordinates, the lower (grounded) electrode end is labelled 'Left Alignment', while at higher coordinates, the upper (driven) electrode begins, labelled 'Right Alignment'. The gap between the electrodes was scanned in 1-micron steps, and both the left alignment (9 microns) and the right alignment (28 microns) are smaller than the approximately 38 microns width of the argon laser, and therefore below the desired limit. The position of the laser was once again

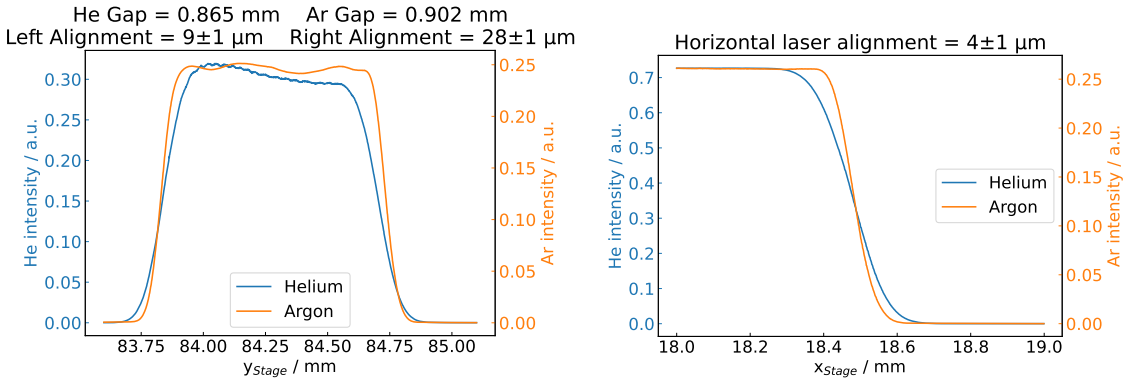

(a) (b)

Figure 4.5: The (a) vertical laser alignment at both electrodes with the gap sizes of the discharge volume of both lasers and (b) horizontal laser alignment. Both alignments are below the desired minimum.

assumed to be at the position where the intensity reaches 50% of the maximum signal. Due to the quartz window, the maximum intensity fluctuates significantly more than without it (as in the measurements of the beam width), which is why the determination of the position is less accurate. This may be due to dust and dirt settling on the window. This systematic error is not included in the figure.

Figure 4.5a also illustrates the distance between the electrodes for both lasers. For the helium and argon lasers, these values correspond not very well with a discrepancy of at least 10% to the gap of 1 mm that the plasma jet should have. The discrepancy between the helium and argon gaps is presumingly due to the different sizes of the laser beams. The overall discrepancy could be because of manufacturing errors or the lack of optimal adjustment of the aforementioned factors. It is also possible that imperfect horizontalisation of the individual beams (see section 4.2) may be a contributing factor.

Figure 4.5b illustrates the horizontal alignment of the laser beams. As previously described, the jet, this time the upper electrode, was guided into the beam in the x-direction. As described above, this is much more important than the vertical alignment and the laser alignment here is also well below the threshold of 38 microns at a beam width of 4 microns.

5. Measurements

The general theory for determining the density of metastable atoms has been explained in section 2.3. However, in practice, a few additional steps are required. These steps result in further systematic uncertainties in the density. The errors shown in the plots are not the total errors. This chapter will elucidate how the errors in the plots arise and the reason for other potential errors.

Normally, the plasma jet is operated with helium for 30 minutes before the measurement to heat the electrodes and ensure the thermal equilibrium of the discharge, thus providing comparable results between different experiments. This was also done here, but thermal equilibrium was not achieved during the measurement, as the plasma had to be switched repeatedly on and off to completely carry out the four measurement series described in Section 2.3. The plasma power decreased during the approximately two-second signal measurement with the laser and plasma switched on I_{PL}, which also affects the metastable atom density. This made it challenging to adjust the power and introduced a systematic error of about $\pm$ 0.05 W. In contrast, the measurement with the laser off and plasma switched on I_P was less affected by this, as the luminosity of the plasma remained approximately constant during the measurement.

Parallel to the heating process the gas lines were flushed with helium to get rid of deposited molecules of water and from the ambient air, which diffuses into the pipes when the gas flow is turned off.

Furthermore, the laser signal's frequency range was verified. This was accomplished by measuring the laser range with the Fabry-Pérot before each series of measurements. Additionally, the ratio of the laser diode current to frequency was evaluated to ensure its accuracy. As the laser controller can only transfer one x-axis to the computer, and both lasers must be tuned parallel, the helium laser must also be tuned to the current ramp of the argon laser. For the helium laser, this resulted in a frequency change of 4.515

GHz/mA for the 8 mA ramp of the argon laser. This corresponds to a frequency range of 36.12 GHz and a frequency change of 0.602 GHz/mA for the 60 mA ramp of the helium laser. A frequency change of 8.3 GHz/mA was observed for the argon laser, which corresponds to a frequency range of 66.7 GHz. These values deviate slightly from the specifications provided by the manufacturer of the laser diodes in Table 3.1. However, the deviation of the frequency ranges between measurement days was under 1%, suggesting that a check may not be necessary before each series of measurements.

Following the measurement of the four signals generated by the plasma on/off and laser on/off settings (where the lasers have not been deactivated, but the shutter has been moved into the beam paths), the LabView program uses these to calculate the absorption signal and then applies a Lorentz fit. Figure 5.1a illustrates the signals for argon with the laser switched on (since the measurements with the laser switched off are only background noise, the display was omitted here). Figure 5.1b shows the resulting absorption curve including fit. The fits have four degrees of freedom for evaluation later. The y-axis intercept y_0, the position of the maximum x_0, the full width at half maximum w and the area under the curve a, which is ultimately used to calculate the density. The formula for the helium fit is a superposition of two Lorentzians with a spacing of 2.67 GHz and a relative signal strength of 0.6 [26]

$$y_0 + \frac{2aw}{\pi} \cdot \left(\frac{1}{4(x - x_0)^2 + w^2} + \frac{0.6}{4(x - x_0 + 2.67)^2 + w^2} \right) \tag{5.1}$$

and the argon fit is a single component without superposition

$$y_0 + \frac{2aw}{\pi} \cdot \frac{1}{4(x - x_0)^2 + w^2}. \tag{5.2}$$

The density is calculated from the area a obtained from the fit, using the formula given in Equation 2.10. The absorption length of the discharge is employed for this purpose. The plasma jet has a width of 1 mm, but the lasers are not guided vertically through the discharge channel, which results in an absorption length of 1.089 mm estimated with Thale's theorem from the distance of the position of the plasma jet to the focussing lens.

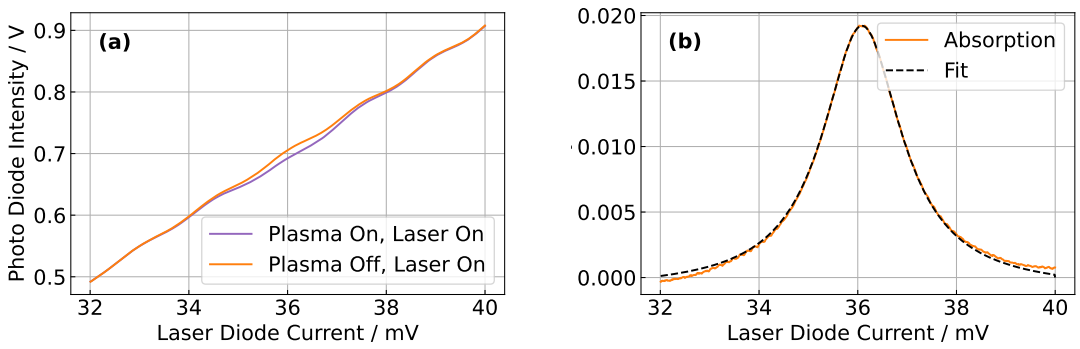

Figure 5.1: Depiction of (a) the I_{LP} and I_P signals and (b) the resulting absorption peak with the Lorentzian fit as an example for argon.

In conjunction with the R^2 value of the fit, the density is transmitted to a Python script, which checks for if either the quality of the fit of the absorption curve R^2 is below 0.8 or for if the peak position or FWHM deviates significantly from realistic values. All densities, whiches absorption curves and fits did not pass this check will then not be taken into account for further analysis. The densities that did pass the check were additionally approved manually. It is crucial to recognise that the quality of the fit also affects the error in the metastable atom densities. This error is not represented in the plots and should add an uncertainty of about 10%.

The measurement of the density is then carried out for different vertical positions between the electrodes of the plasma jet with a resolution of 50 microns. All densities, where absorption curves and fits did pass the check are forming a vertical slice as seen in figure 5.2. The densities of the metastable atoms of helium and argon are plotted against the distance to the powered electrode. One can see that for both the helium and the argon densities some data points are missing near the electrodes. These are the ones sorted out as mentioned above.

To get a two-dimensional map of the discharge channel these vertical slices are done for different distances to the nozzle of the jet. The horizontal resolution is 1 mm. Figure 5.3 illustrates an interpolated map for a pure helium discharge. Here the discharge

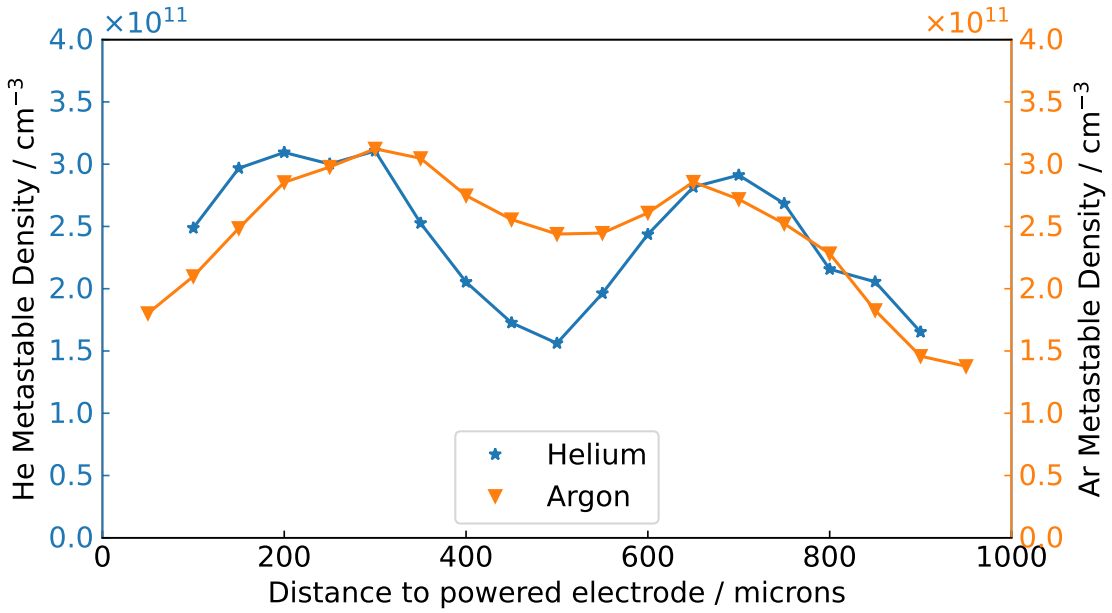

Figure 5.2: Example of a vertical slice of He $^3S_1$ (blue) and Ar $^3P_2$ (orange) metastable atom densities for 1.1 W dissipated in the helium discharge with 0.05% argon.

channel up to 9 mm distance to the nozzle can be seen. The nozzle is at position 0, the discharge channel is in negative coordinates and the effluent would be in positive coordinates (COST-Jet conventions [5]). Some dynamics are already discernible and will be discussed in greater detail subsequently. The density is now shown in different colours respective to their values. Two layers with a higher density of metastable helium atoms can be identified at 200–400 microns with up to $2.5{\cdot}10^{12}$ cm^{-3} and 600–800 microns with a bit fewer metastable atoms at about $2{\cdot}10^{12}$ cm^{-3}. These layers form due to the higher electron densities directly in front of the sheaths as discussed in section 2.1.2. The slightly lower metastable atom density near the sheath of the grounded electrode is because the electron density is lower at this sheath [44]. Between these layers the density drops to about $1.7{\cdot}10^{12}$ cm^{-3} and directly at the electrodes the density falls to about $1{\cdot}10^{12}$ cm^{-3}. Moreover, the density of metastable helium atoms is significantly lower at the nozzle. This phenomenon can be attributed to the back diffusion of the ambient air atmosphere, the particles of the ambient air quenching the metastable atoms.

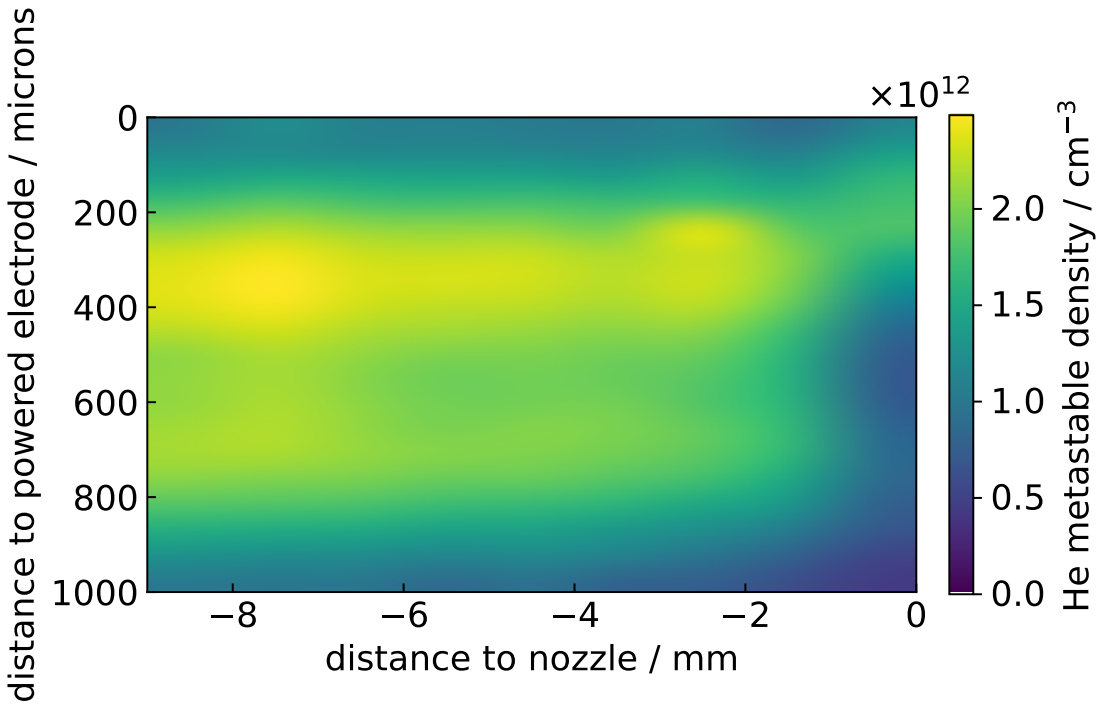

Figure 5.3: Interpolated He $^3S_1$ metastable density map of the near effluent region of a pure helium discharge at 1 W.

Since measuring one verticle slice takes about 10 minutes, generating one of the two-dimensional maps requires several hours, so only one verticle slice was measured for systematic parameter variations. The distance from the nozzle was set at -10 mm, as the atmosphere exerts minimal influence on the density of metastable atoms. To compare dozens of slices for parameter variations would be impracticable, therefore one density is calculated as representative of one slice and subsequently for one set of parameters. This density is the mean of the maximum density of the slice and its two neighbours provided that both neighbouring densities fulfil the criteria for R^2, peak position and FWHM as mentioned above. This is done to ensure that a vertical slice has at least three neighbouring successful densities to be considered. Also, the position of the maximum density will not be exactly the position of the density, but between it and its neighbours. If one of the neighbours of the maximum density does not meet the conditions mentioned above, the second-highest density is then examined, and so on. The error associated with the mean

value of the density and its neighbours is represented by the error shown in the figures in the following sections. The number of invalid densities in a slice is not considered. The probability of the maximum density deviating from the real maximum increases as the number of valid densities decreases. However, this should be less of an issue as the lower densities are falling below the detection limit are the ones that are sorted out most frequently.

5.1 Gas Mixture Variations

In the previous section, it was observed that back diffusion of other particles than helium in a helium discharge has a major influence on the density of helium metastable atoms. With the parameter variations introduced in chapter 1 from [3] in mind the helium and argon metastable densities were measured for controlled introduction of argon into the helium discharge.

Figure 5.4 illustrates the densities of metastable helium and argon atoms as a function of the proportion of argon in the feed gas on the left y-axis. The maximum helium metastable density of about $1.5{\cdot}10^{12}$ cm^{-3} is in a pure helium discharge. With a small argon admixture of 0.02% the helium metastable density drops down to less than half of this value and the argon metastable atoms are immediately measurable with a density of about $2.5{\cdot}10^{11}$ cm^{-3}. With rising argon admixture, the helium metastable density drops until it falls under the detection limit after 0.7% argon admixture. On the other hand, the argon metastable atom density is rising, at a higher density than helium at about 0.05% admixture. The increase stagnates between 0.2% and 0.4% argon admixture, which is measured in many data sets of argon admixture variation, but it is not yet clear if this is an artefact or a real behaviour of the metastable argon atoms, having its maximum at 1% with a density of $1.6{\cdot}10^{12}$ cm^{-3}, even higher than the maximum helium density. The slope of the argon density indicates higher values beyond 1%, which was impossible to measure because the plasma begins to arc with more argon admixture. The metastable state of argon is more favourable in the discharge due to the lower excitation energy of 11.55 eV in contrast to the 19.82 eV of helium, having a higher cross section for all

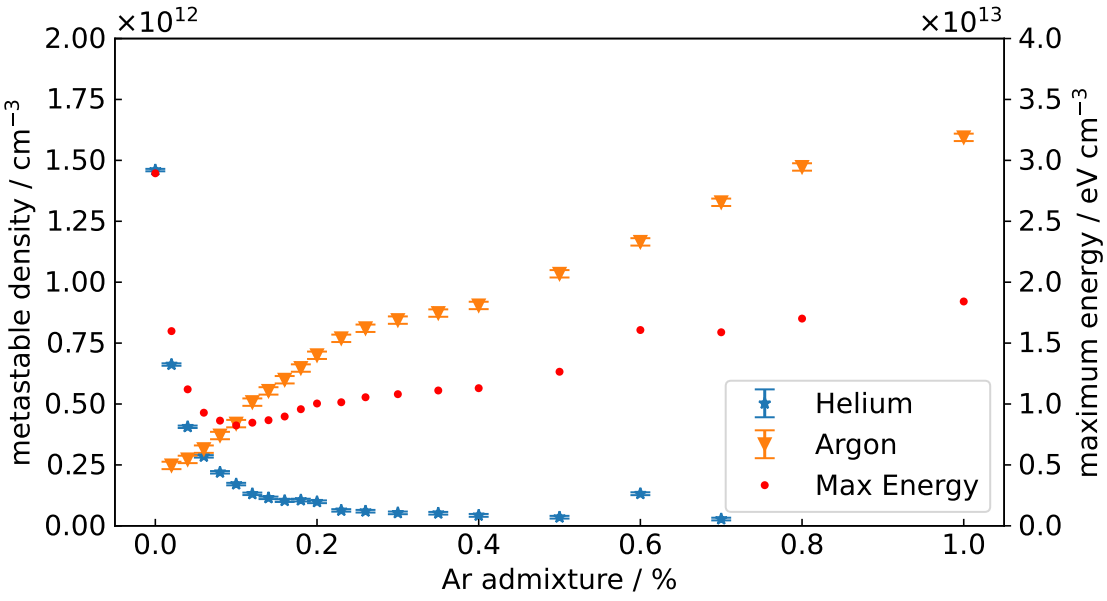

Figure 5.4: He $^3S_1$ (blue) and Ar $^3P_2$ (orange) metastable atom densities as a function of Ar admixture to the feed gas for 1.1 W dissipated in the discharge. The total gas flow is 1000 sccm. The red dots indicate the maximum potential energy for the helium and argon metastable states.

electron energies [45]. On the one hand, the probability of an argon atom colliding with an electron increases with higher argon admixture. On the other hand, the ionisation rate also increases, as not only is the metastable state preferred, but the ionisation of argon is also more efficient than helium due to the lower ionisation energy.

Comparing the densities of the two-dimensional map in Figure 5.3, which illustrates the density of metastable atoms in a pure helium discharge, with a maximum density of $2.5{\cdot}10^{12}$ cm^{-3} to the variation of argon admixture, exhibiting a maximum density of $1.5{\cdot}10^{12}$ cm^{-3} at 0% argon, the mapping measurement was performed at 0.1 W less power, but the density is higher. This is likely due to the presence of impurities that differ between the two measurements. The absolute values are approximately one to two orders of magnitude larger than those observed in other atmospheric plasma jets (introduced in [46] and advanced in [47]), as reported in [8] with the same measurement technique being TDLAS. However, our discharge contains fewer impurities, which also

could account for this discrepancy.

In the context of CO_2 dissociation, it is challenging to ascertain whether the metastable atoms exert a significant influence. One indication is the maximum potential energy contained in the metastable atoms

$$\varepsilon_{max} = n_{He^*} \cdot 19.82eV + n_{Ar^*} \cdot 11.55eV \tag{5.3}$$

that could be transferred to the CO_2 molecules. This is indicated in red in figure 5.4. The maximum energy at one per cent argon in the discharge remains below the energy in a pure helium plasma. Measurements from Niermann [8] indicate that the maximum argon density has its highest value at 4% and is approximately twice as high as at 1%. Notwithstanding this supposition, the observed increase in CO_2 conversion in figure 1.1a from [3] would require a maximum energy of $5.7{\cdot}10^{13}$ eV cm^{-3} and therefore an argon density of about $5{\cdot}10^{12}$ cm^{-3}. Nevertheless, this is merely conjecture, given that CO_2 in the discharge will significantly alter the properties of the discharge itself.

5.2 Power Variations

The second parameter varied is the dissipated power in the discharge. Figure 5.5a depicts the densities of metastable helium and argon atoms plotted against power, with an argon admixture of 0.02%. The helium metastable atoms are at a density of about $1.2{\cdot}10^{11}$ cm^{-3} at 0.3 W power dissipated in the discharge and is linear increasing up to about $6{\cdot}10^{11}$ cm^{-3} at 1.1 W. The argon metastable atoms are also linear increasing from $0.7{\cdot}10^{11}$ cm^{-3} at 0.3 W up to $2.5{\cdot}10^{11}$ cm^{-3} at 1.1 W. The linear behaviour can be explained by the fact that the density of metastable atoms depends on the electron density, which in turn is proportional linear to the power [31].

Figure 5.5b shows the same variation for 0.1% argon admixture. Here the helium metastable atom density is lower than at 0.02% (which was already observed above), but also the slope is lower than for the lower argon admixture case, dropping from about $4.8{\cdot}10^{11}$

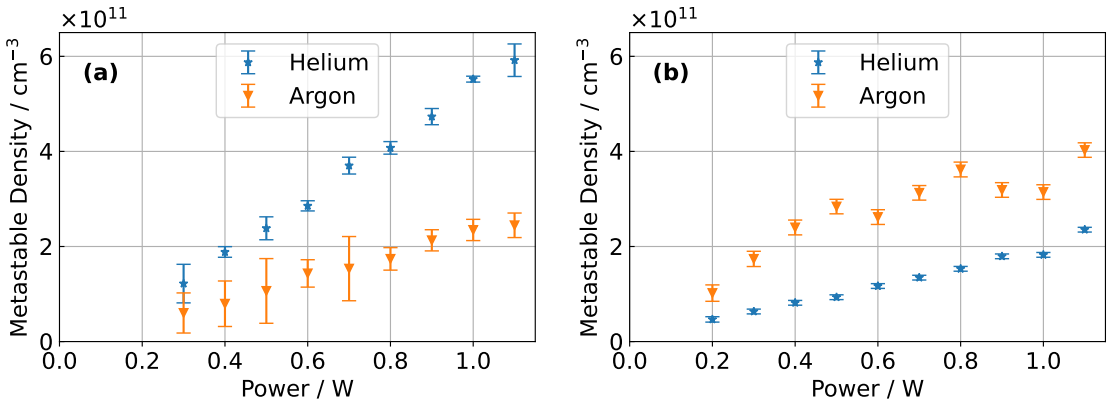

Figure 5.5: He $^3S_1$ (blue) and Ar $^3P_2$ (orange) metastable atom densities as a function of power for (a) 0.02% and (b) 0.1% argon in the helium feed gas.

cm^{-3} / 0.8 W to about 2·10^{11} cm^{-3} / 0.8 W. The opposite can be seen for the argon metastable density, whiches increase is higher with more argon admixture.

5.2.1 Vertical Profiles

Looking closer into the verticle slices of the power variation with 0.02% argon of figure 5.5a one can see that the verticle position of the maximum helium and argon metastable densities are changing with power. This is depicted in figure 5.6 for some powers exemplary. For 0.3 W both helium and argon metastable density maxima are in the middle between the electrodes at approximately 400-600 microns. With higher power, the width of the maximum density increases and is now between 300-700 microns. The helium metastables begin to form the two layers already observed in the two-dimensional map in figure 5.3. For high powers (1.0 W) both helium and argon metastable atoms form two layers in front of the sheaths at the electrodes at about 200-300 and 600-700 microns. This behaviour is typically for a helium-dominated discharge. As outlined in section 2.1.2 the electron density is highest in the bulk of the plasma for lower powers and shifts to the sheaths as the discharge changes from Ω-dominated behaviour to Penning-dominated behaviour at high powers. What is not understood is that the argon metastable atoms seem to be shifting to the sheaths at higher powers than the helium metastable atoms. The excitation of argon metastable atoms should be favoured for all electron energies,

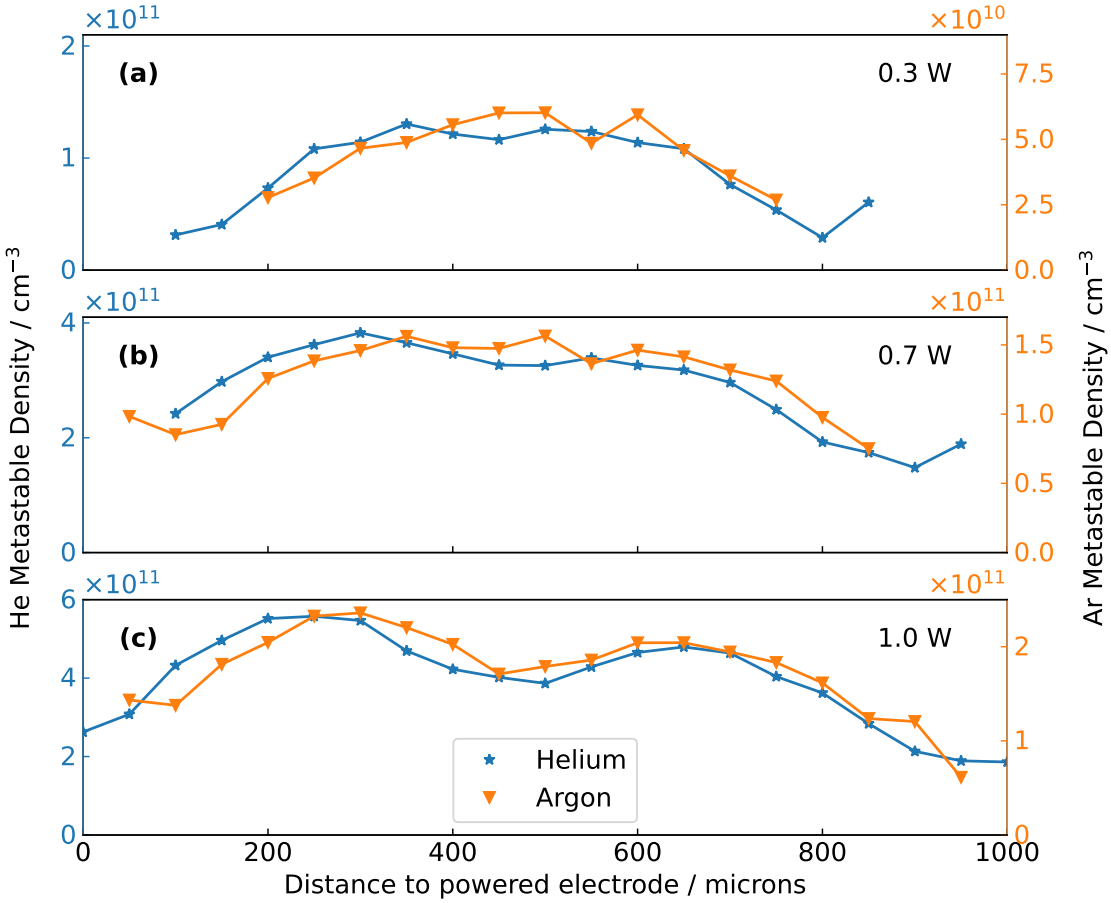

Figure 5.6: Vertical slices of He $^3S_1$ (blue) and Ar $^3P_2$ (orange) metastable atom densities for (a) 0.3 W, (b) 0.7 W and (c) 1.0 W dissipated in a helium discharge with 0.02% argon.

as the cross section for this state is higher at all electron energies [45]. But the helium and argon atoms are interacting together and also with the electrons, which is a highly complicated system with many possible reactions.

For higher argon admixtures the behaviour of the metastable atoms to shift to the layers is completely different. In figure 5.7 the vertical slice of an argon admixture of 0.1% at 0.4 W is shown for the helium metastable density. The data on the argon density is in the range of the detection limit and can therefore not be interpreted. But what is visible is that at this higher argon admixture, the helium metastable atoms are already at this

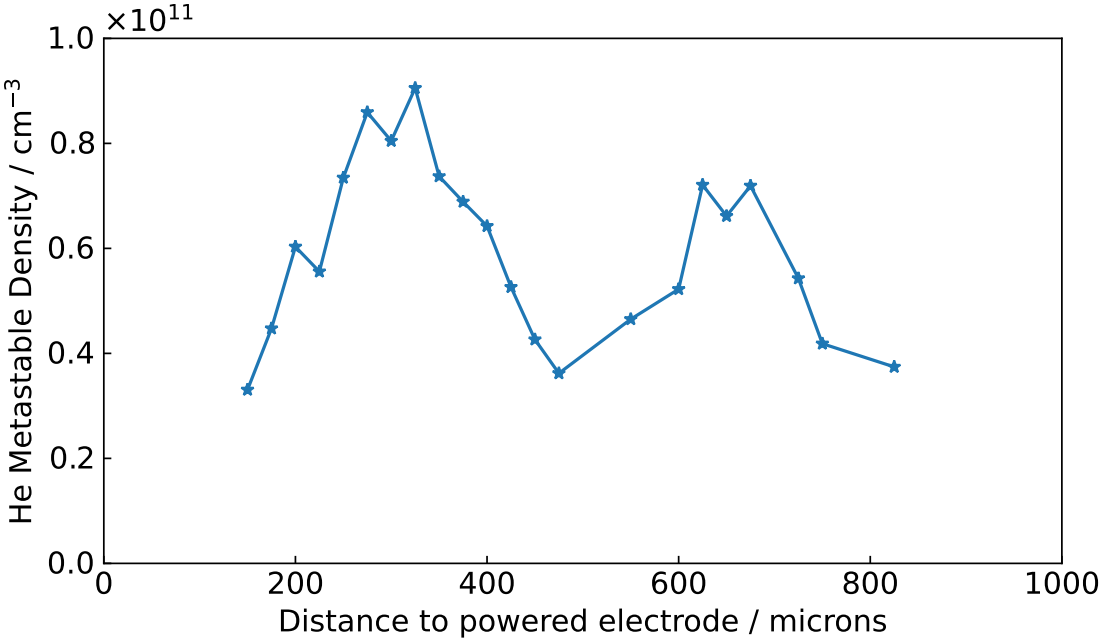

Figure 5.7: Vertical slice of He $^3S_1$ metastable atom densities for 0.4 W dissipated in the helium discharge with 0.1% argon.

low power of 0.4 W shifted to the layers at about 300 microns and supposedly at 700 microns. This behaviour is typical for an argon-dominated discharge [19].

6. Conclusion

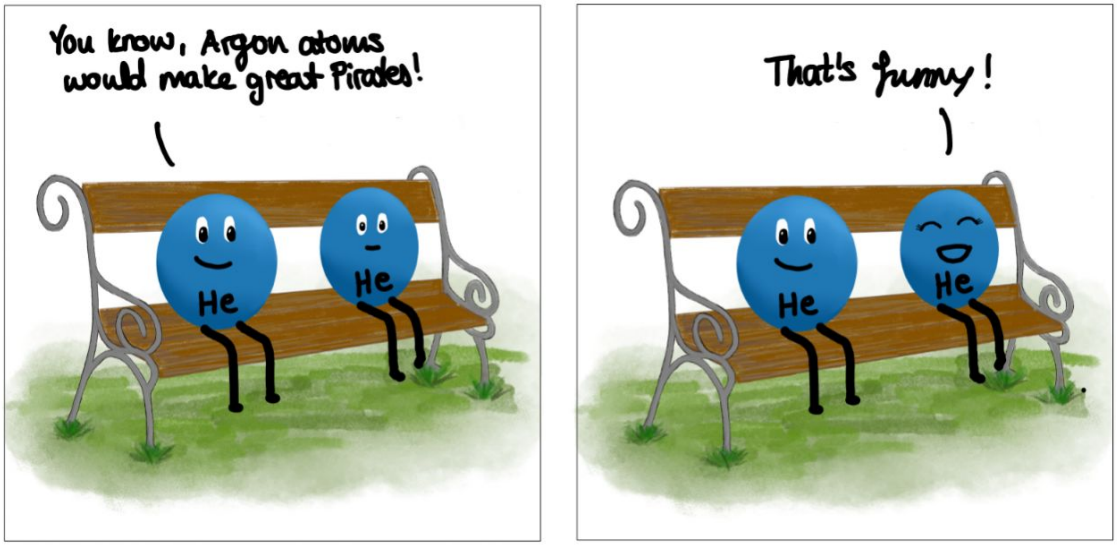

In this study, the densities of the He $^3S_1$ and Ar $^3P_2$ metastable states were quantified in response to variations in power and argon addition within a helium radio frequency (rf) atmospheric pressure plasma. The two metastable states were simultaneously excited by two tunable diode lasers and subsequently measured by absorption spectroscopy (TDLAS). A particular focus was placed on the spatial distribution of the metastable atoms, which was made possible by a plasma source that could be moved by stepper motors.

The most significant challenge was to modify the previously employed setup for measuring a single species to accommodate both states simultaneously. The capacity to measure both metastable states simultaneously enables a more accurate comparison of the densities of metastable helium and argon. The ratios and progression of the densities of both states provide a reliable comparative measurement for comparison with a discharge involving a mixture of CO_2.

It can be observed that even small admixtures of argon, at a concentration of 0.02%, have a significant effect on the metastable densities of the discharge. The density of metastable helium is reduced by approximately 50%. From an admixture of 0.05%, the density of metastable argon is higher than that of helium, which continues to fall with increasing argon admixture until it is no longer measurable from 0.7% argon admixture. The density of metastable argon continues to increase. A comparison of the present results with those obtained from older measurements in comparable rf atmospheric pressure plasma jets indicates that the present density is one order of magnitude higher [31] presumably because of lesser impurities.

Further insights are then provided by the power variations, which show a linear increase in both densities with higher power. However, the gradient depends on the admixture. For instance, the density of metastable argon atoms exhibits a more pronounced increase when the power is elevated in the presence of a higher argon admixture, whereas the density of helium atoms displays a comparatively weaker increase. The linear increases are consistent with measurements of the electron density, which is responsible for the generation of metastable atoms and also increases linearly with increasing power.

However, it is not only the densities that change with different power levels but also the spatial distribution of metastable atoms. The spatial distribution of the metastable atoms undergoes a similar change to that observed in a discharge in which pure helium is added when argon is added in admixtures of 0.02%. The densities of metastable atoms (and, consequently, electrons) are highest in the bulk of the discharge, with a shift towards the electrodes at higher power levels. At admixtures of only 0.1%, the densities of metastable helium are at their maximum at the electrodes even at low power levels. This is a typical phenomenon observed in discharges with pure argon [19]. It can be concluded that admixtures of 0.1% are sufficient to alter the dynamics of the discharge in a manner that resembles a pure argon discharge.

These findings are not unexpected, given that the energy of the metastable state and the ionisation energy are lower for argon. Consequently, cross-sections are higher across all electron energies, with argon being preferentially excited and ionised.

This work successfully obtained simultaneously and spatially resolved measurements of the densities of the He $^3S_1$ and Ar $^3P_2$. These can be taken as a baseline to be repeated and compared later with an admixture of CO_2. It is anticipated that this will facilitate further comprehension of the discharge and CO_2 dissociation processes.

6.1 Problems and Opportunities for Improvement

The overall configuration is stable, and the measurements are proceeding as anticipated. However, there are a few areas that could be enhanced:

Adjusting the post holders: The post holders utilised in this configuration were equipped with a single locking screw. All adjustments were conducted manually. Had precision screws been employed, a significant reduction in the required adjustment time could have been achieved, with the alignment of the beams potentially being set with greater precision. Nevertheless, this should have a negligible impact on the densities of metastable atoms.

Background frequencies: This issue has not yet been addressed, but it can be observed in Figure 5.1a. The intensity does not increase linearly, as it should. Some oscillation has been superimposed on the laser signal. The oscillations did not affect the absorption curves at the time of the measurements presented in this thesis, so it should not have a significant effect on the densities of the metastable atoms. However, the setup was changed slightly after the measurements (the mount for the plasma jet was replaced). Since then, the oscillations can be seen very clearly in the absorption curves. At the time of writing, the cause of this intensity could not be identified. Nevertheless, these oscillations do not appear to be proportional to the intensity at the photodiode. The intensity of the frequency decreases relative to the intensity coming from the laser.

Higher photodiode intensity: A further issue that arises concerning the previous problem is the necessity for diodes that can measure a higher intensity without saturating. This is because a better signal-to-noise ratio is possible, but it is important

to ensure that the resolution does not deteriorate, as the absorption of the plasma is already low.

6.2 Outlook

In the future, it will be necessary to make measurements at higher argon admixtures. This will demonstrate whether the density of the metastable argon density continues to increase or reaches a maximum at some point. The work of Niermann indicates this for argon, but during the argon measurements, the discharge highly changed due to impurities [8]. It would also be of interest to observe further variations in power with argon admixtures between the helium-dominant discharge and the argon-dominant discharge, which could give more information on the transition between these extremes. Finally, measurements with CO_2 admixture will be of interest in answering the original question of the role of metastable atoms for CO_2 dissociation.

Bibliography

[1] S. Renninger, M. Lambarth, and K. P. Birke, "High efficiency CO2-splitting in atmospheric pressure glow discharge," *Journal of CO2 Utilization*, vol. 42, p. 101322, Dec. 2020.

[2] L. F. Spencer and A. D. Gallimore, "Efficiency of CO2 Dissociation in a Radio-Frequency Discharge," *Plasma Chemistry and Plasma Processing*, vol. 31, pp. 79–89, Feb. 2011.

[3] C. Stewig, S. Schüttler, T. Urbanietz, M. Böke, and A. Von Keudell, "Excitation and dissociation of CO_2 heavily diluted in noble gas atmospheric pressure plasma," *Journal of Physics D: Applied Physics*, vol. 53, p. 125205, Mar. 2020.

[4] T. Urbanietz, M. Böke, V. Schulz-von Der Gathen, and A. Von Keudell, "Non-equilibrium excitation of CO_2 in an atmospheric pressure helium plasma jet," *Journal of Physics D: Applied Physics*, vol. 51, p. 345202, Aug. 2018.

[5] J. Golda, J. Held, B. Redeker, M. Konkowski, P. Beijer, A. Sobota, G. Kroesen, N. S. J. Braithwaite, S. Reuter, M. M. Turner, T. Gans, D. O'Connell, and V. Schulz-von Der Gathen, "Concepts and characteristics of the 'COST Reference Microplasma Jet'," *Journal of Physics D: Applied Physics*, vol. 49, p. 084003, Mar. 2016.

[6] G. Isbary, J. Heinlin, T. Shimizu, J. Zimmermann, G. Morfill, H. Schmidt, R. Monetti, B. Steffes, W. Bunk, Y. Li, T. Klaempfl, S. Karrer, M. Landthaler, and W. Stolz, "Successful and safe use of 2 min cold atmospheric argon plasma in chronic wounds: results of a randomized controlled trial," *British Journal of Dermatology*, vol. 167, pp. 404–410, Aug. 2012.

[7] M. Leimkühler, "Erzeugung von Metastabilen mit Hilfe von kHz-getriebenen Mikroplasma-Arrays," Master's thesis, RUB, 2018.

[8] B. Niermann, M. Böke, N. Sadeghi, and J. Winter, "Space resolved density measurements of argon and helium metastable atoms in radio-frequency generated He-Ar micro-plasmas," *The European Physical Journal D*, vol. 60, pp. 489–495, Dec. 2010.

[9] A. A. Fridman and L. A. Kennedy, *Plasma physics and engineering*. New York: Taylor & Francis, 2004.

[10] S. Spiekemeier, *Transient metastable dynamics in atmospheric pressure microplasma jets*. PhD thesis, RUB, 2016.

[11] E. Marode, "The mechanism of spark breakdown in air at atmospheric pressure between a positive point and a plane. I. Experimental: Nature of the streamer track," *Journal of Applied Physics*, vol. 46, pp. 2005–2015, May 1975.

[12] S. Kelly, J. Golda, M. M. Turner, and Volker Schulz-von Der Gathen, "Gas and heat dynamics of a micro-scaled atmospheric pressure plasma reference jet," *Journal of Physics D: Applied Physics*, vol. 48, p. 444002, Nov. 2015.

[13] Y. Raizer, *Gas Discharge Physics*. Springer International Publishing, 1991.

[14] J.-W. Lackmann, S. Schneider, E. Edengeiser, F. Jarzina, S. Brinckmann, E. Steinborn, M. Havenith, J. Benedikt, and J. E. Bandow, "Photons and particles emitted from cold atmospheric-pressure plasma inactivate bacteria and biomolecules independently and synergistically," *Journal of The Royal Society Interface*, vol. 10, p. 20130591, Dec. 2013.

[15] R. Rahul, O. Stan, A. Rahman, E. Littlefield, K. Hoshimiya, A. P. Yalin, A. Sharma, A. Pruden, C. A. Moore, Z. Yu, and G. J. Collins, "Optical and RF electrical characteristics of atmospheric pressure open-air hollow slot microplasmas and application to bacterial inactivation," *Journal of Physics D: Applied Physics*, vol. 38, pp. 1750–1759, June 2005.

[16] A. Lührmann, R. Matthes, and A. Kramer, "Impact of cold atmospheric pressure argon plasma on antibiotic sensitivity of methicillin-resistant Staphylococcus aureus strains in vitro," *GMS Hygiene and Infection Control*, vol. 11, p. Doc17, Aug. 2016. Publisher: German Medical Science GMS Publishing House.

[17] D. W. Liu, F. Iza, and M. G. Kong, "Electron heating in radio-frequency capacitively coupled atmospheric-pressure plasmas," *Applied Physics Letters*, vol. 93, p. 261503, Dec. 2008.

[18] T. Hemke, D. Eremin, T. Mussenbrock, A. Derzsi, Z. Donkó, K. Dittmann, J. Meichsner, and J. Schulze, "Ionization by bulk heating of electrons in capacitive radio frequency atmospheric pressure microplasmas," *Plasma Sources Science and Technology*, vol. 22, p. 015012, Dec. 2012.

[19] J. Golda, J. Held, and V. S.-v. D. Gathen, "Comparison of electron heating and energy loss mechanisms in an RF plasma jet operated in argon and helium," *Plasma Sources Science and Technology*, vol. 29, p. 025014, Feb. 2020.

[20] D. Schröder, S. Burhenn, T. De Los Arcos, and V. Schulz-von Der Gathen, "Characteristics of a propagating, self-pulsing, constricted ' gamma-mode-like' discharge," *Journal of Physics D: Applied Physics*, vol. 48, p. 055206, Feb. 2015.

[21] C. Gerry and P. Knight, *Introductory Quantum Optics*. Cambridge [Cambridgeshire] ; New York : Cambridge University Press, 2005.

[22] S. S. Hodgman, R. G. Dall, L. J. Byron, K. G. H. Baldwin, S. J. Buckman, and A. G. Truscott, "Metastable Helium: A New Determination of the Longest Atomic Excited-State Lifetime," *Physical Review Letters*, vol. 103, p. 053002, July 2009.

[23] Sahin, I. Tapan, E. N. Özmutlu, and R. Veenhof, "Penning transfer in argon-based gas mixtures," *Journal of Instrumentation*, vol. 5, pp. P05002–P05002, May 2010.

[24] F. Massines, A. Rabehi, P. Decomps, R. B. Gadri, P. Ségur, and C. Mayoux, "Experimental and theoretical study of a glow discharge at atmospheric pressure controlled by dielectric barrier," *Journal of Applied Physics*, vol. 83, pp. 2950–2957, Mar. 1998.

[25] M. A. Lindon and E. E. Scime, "CO $_2$ dissociation using the Versatile atmospheric dielectric barrier discharge experiment (VADER)," *Frontiers in Physics*, vol. 2, Sept. 2014.

[26] "NIST: Atomic Spectra Database Lines Form," *https://physics.nist.gov/PhysRefData/ASD/lines_form.html*, Dec. 2023.

[27] J. M. Pouvesle, J. Stevefelt, and C. B. Collins, "Study of two-body and three-body channels for the reaction of metastable helium atoms with nitrogen," *The Journal of Chemical Physics*, vol. 82, pp. 2274–2279, Mar. 1985.

[28] B. Niermann, A. Kanitz, M. Böke, and J. Winter, "Impurity intrusion in radio-frequency micro-plasma jets operated in ambient air," *Journal of Physics D: Applied Physics*, vol. 44, p. 325201, Aug. 2011.

[29] N. Sadeghi, "6. Molecular Spectroscopy Techniques Applied for Processing Plasma Diagnostics," *Journal of Plasma and Fusion Research*, vol. 80, no. 9, pp. 767–776, 2004.

[30] W. Demtröder, *Laser Spectroscopy 1*. Berlin, Heidelberg: Springer Berlin Heidelberg, 2014.

[31] B. Niermann, *The role of metastable atoms in radio-frequency micro-plasma jet discharges operated at atmospheric pressure*. PhD, RUB, 2011.

[32] L. F. Cohen-Tannoudji C., Diu B., *Quantum mechanics*, vol. Volume 1. WILEY-VCH, 1996.

[33] A. Corney, *Atomic and laser spectroscopy*. Oxford classic texts in the physical sciences, Oxford: Clarendon Press, 2006.

[34] K. Niemi, J. Waskoenig, N. Sadeghi, T. Gans, and D. O'Connell, "The role of helium metastable states in radio-frequency driven helium–oxygen atmospheric pressure plasma jets: measurement and numerical simulation," *Plasma Sources Science and Technology*, vol. 20, p. 055005, Oct. 2011.

[35] V. A. Godyak and R. B. Piejak, "*I n s i t u* simultaneous radio frequency discharge power measurements," *Journal of Vacuum Science & Technology A: Vacuum, Surfaces, and Films*, vol. 8, pp. 3833–3837, Sept. 1990.

[36] J. Held, "mimurrayy/COST-power-monitor," *https://github.com/mimurrayy/COST-power-monitor*, Dec. 2023. original-date: 2018-07-04T15:42:46Z.

[37] W. Demtröder, *Experimentalphysik 3*. Springer-Lehrbuch, Berlin, Heidelberg: Springer Berlin Heidelberg, 2016.

[38] M. W. Sigrist, *Laser: Theorie, Typen und Anwendungen*. Berlin, Heidelberg: Springer Berlin Heidelberg, 2018.

[39] "Lead-Salt Semiconductor Lasers," *https://www.fiberoptics4sale.com/blogs/wave-optics/lead-salt-semiconductor-lasers*, Apr. 2024.

[40] G. Hernandez, *Fabry-Perot interferometers*. Cambridge [Cambridgeshire] ; New York : Cambridge University Press, 1986.

[41] Y.-J. Rao, Z.-L. Ran, and Y. Gong, *Fiber-optic fabry-perot sensors: an introduction*. Series in fiber optic sensors, Boca Raton London New York: CRC Press, Taylor & Francis Group, 2017.

[42] M. A. De Araújo, R. Silva, E. De Lima, D. P. Pereira, and P. C. De Oliveira, "Measurement of Gaussian laser beam radius using the knife-edge technique: improvement on data analysis," *Applied Optics*, vol. 48, p. 393, Jan. 2009.

[43] Köchner, *Solid-State Laser Engineering*. No. 1 in Springer Series in Optical Sciences, Springer-Verlag New York, 2006.

[44] J. Golda, F. Kogelheide, P. Awakowicz, and V. S.-v. D. Gathen, "Dissipated electrical power and electron density in an RF atmospheric pressure helium plasma jet," *Plasma Sources Science and Technology*, vol. 28, p. 095023, Sept. 2019.

[45] L. Alves, "The IST-Lisbon database on LXCat'," *J. Phys. Conf*, vol. 565, no. 1, 2014.

[46] A. Schutze, J. Jeong, S. Babayan, Jaeyoung Park, G. Selwyn, and R. Hicks, "The atmospheric-pressure plasma jet: a review and comparison to other plasma sources," *IEEE Transactions on Plasma Science*, vol. 26, pp. 1685–1694, Dec. 1998.

[47] V. Schulz-von Der Gathen, L. Schaper, N. Knake, S. Reuter, K. Niemi, T. Gans, and J. Winter, "Spatially resolved diagnostics on a microscale atmospheric pressure plasma jet," *Journal of Physics D: Applied Physics*, vol. 41, p. 194004, Oct. 2008.

Thanks

Well well well, this thesis comes to a close, and so is my master's programme. But not without a big shoutout to all the people who helped me through all these years.

- Firstly I want to thank Jun.-Prof. Judith Golda, for that I could do this research.
- Then I would like to thank Dr. Marc Böke, for being the second reviewer.
- Dr Sebastian Burhenn was a fine supervisor in the first half of this project.
- Dr Volker Schulz-von der Gathen, Dr Marc Böke and (soon-to-be doctors) Sascha Chur and Steffen Schüttler gave me advice during the writing of this thesis. Especially Volker saved me from making some grave mistakes ;)
- The technicians Kai Fiegler, Björn Redeker, Michael Konkowski and Axel Lang all helped me to be able to set up the experiment.
- I want to thank the rest of all the people of EP II for the amazing working atmosphere and who supervised me collectively in the second half of the project.
- My roommates Lennart Ahrens and Katharina Leitmann (who drew the crazy good comics for me) both had to live with my humour.
- Lastly I want to thank all the other people who supported me. Especially the old Siegen-Gang, who were sometimes the only reason that I showed up at university during my bachelor :D

Many many thanks!